HELIUM AND MINOR IONS IN THE CORONA AND SOLAR WIND: DYNAMICS AND CHARGE STATES

A. BÜRGI* and J. GEISS

Physikalisches Institut, University of Bern, Sidlerstrasse 5, CH-3012 Bern, Switzerland

(Received 30 August, 1985)

Abstract. A theoretical model of the acceleration region of the solar wind with major species (p, α, e) and minor ions (e.g., ^{3}He, C, O, Mg, Si) is presented. Observed n_e-profiles and the equations of continuity and momentum are used to calculate profiles of T, n, and u for all species, as well as charge states of minor ions. The disagreement of the results of a pure p–e model with observations is discussed in some detail, and it is shown that a model consistent with observations both in the corona and at 1 AU requires a finite abundance of He^{++}. This model predicts a strong enhancement of He/H in the lower corona. The results for the frozen-in charge states in the p–α–e model are in agreement with measurements in the low speed solar wind, especially for the well determined pair O^{6+}/O^{7+}. Finally, a model for a coronal hole is investigated and it is found that wave pressure is necessary to model successfully the observed solar wind speeds and abundances.

Although various simplifying assumptions had to be introduced, care was taken to ensure that the model remains physically consistent, i.e., that the same physics is used for the major species as well as the minor ions.

1. Introduction

The heavier components in the solar wind provide a set of test particles with widely different mass and charge which can be used to probe the physical conditions in the corona and solar wind.

The study of the dynamics of minor ions helps to delimit possible fractionation processes in the corona which need to be understood in order to relate abundances in the solar wind to those in the Sun itself. However, not only elemental and isotopic abundances are of interest: the distribution of charge states of heavy elements carries important information as well. In contrast to other parameters, e.g., density, velocity, or temperature, which vary by orders of magnitude between the corona and 1 AU, the charge state distribution is 'frozen-in' relatively low in the corona. *In-situ* measurements of charge states in the solar wind can therefore be used to infer the physical state of the low corona. The message contained in the charge states is complex, however, and model calculations have to be invoked for its better understanding.

To date, studies of heavy minor ions have concentrated either on the charge states alone (Hundhausen *et al.*, 1968; Bame *et al.*, 1974; Owocki, 1982; Bochsler, 1983), making simple assumptions concerning the expansion kinetics, or else they have treated the dynamics of ions with fixed charge (Geiss *et al.*, 1970; Nakada, 1970; Joselyn and Holzer, 1978; Borrini and Noci, 1979; McKenzie *et al.*, 1979).

In this work, we synthesize the two approaches and treat the evolution of charge

* Present address: NASA Goddard Space Flight Center, Code 692, Greenbelt, MD 20771, U.S.A.

Solar Physics **103** (1986) 347–383.

states and dynamics simultaneously. Particular emphasis is laid on consistency of the models for minor and major ions, since any *ad hoc* choice in the model for major ions would invalidate the approach. Also, we introduce a generalized thermal force, thus extending thermal diffusion beyond the diffusion approximation by including a heat flow interaction in the collision terms that is applicable for arbitrary velocities.

2. Model Assumptions

We assume:

– A steady state solar wind, i.e., all partial time derivatives are set to zero.

– Equal temperatures for all species. This is of course not the case in the real solar wind at 1 AU, where the temperature of ions has been observed to be roughly mass-proportional (cf. Schmidt *et al.*, 1980; Bochsler *et al.*, 1985). However, the assumption should be a useful approximation in the corona outside coronal holes, where the low-speed solar wind is thought to originate. There the densities are high enough for the plasma to be collision dominated, and temperatures should be near equilibrium at least over the range where charge states are frozen-in. So the charge-state calculations should not be affected much by this assumption, and neither should be the dynamics of ions in the corona. In contrast, we cannot expect the dynamics of ions at large heliocentric distances to be realistic, since there the assumption of equal temperature is known to be false, so solutions beyond $\simeq 10\ R_\odot$ are merely illustrative extrapolations of the coronal models.

We also assume:

– Equal velocities of ions of one species (i.e., an element or isotope). The model thus cannot reproduce the effect of unequal flow speeds for different charge states of the same species (cf. Owocki *et al.*, 1983). Since the speed differences between protons and ions tend to be inversely proportional to Z^2/A (in the diffusion limit, Z being the charge- and A the mass-number of the charge state in question), speed differences will not be too large as long as Z is large. Moreover, there will also be equilibration of speeds between neighbouring charge states by transfer of momentum in ionization/recombination processes below the freezing-in level. The assumption of equal velocities considerably simplifies the system of momentum equations from one for each charge state, each with its own critical point, to a single momentum equation for the mean velocity with a single critical point for each species, and thus greatly reduces computational complexity.

– The flow of protons to be in the radial direction everywhere, in a flux tube which is locally symmetric (except for the spiral angle of the magnetic field at large distances), and whose cross section is given by

$$a(r) = f_a(r)(r/R_\odot)^2, \tag{1}$$

where $f_a(r)$ contains the 'superradial' divergence of the flux tube and is parametrized in the form (Kopp and Holzer, 1976)

$$f_a(r) = \frac{f_m\, e^{(r-r_1)/\sigma_1} + f_1}{e^{(r-r_1)/\sigma_1} + 1}. \tag{2}$$

For the p-α-e-plasma, the problem is now to determine the eight unknown profiles

n_p, n_α, n_e (densities),
u_p, u_α, u_e (velocities),
T (temperature),
E (electric field).

This can be done by using the
- continuity equations for all species (3 equations);
- momentum equations for all species (3 equations);
- condition of charge neutrality (1 equation);
- energy equation for the bulk flow (1 equation).

From these, together with appropriate boundary conditions, the profiles can be determined in principle. However, the energy equation poses some problems:

What should be specified for the electron heat flux?

How can we describe the energy source, which we have to include if we want to model the region of the coronal temperature maximum?

These problems can be circumvented, if we do not use the energy equation, but prescribe instead one of the profiles: In the present work this will be the electron density profile, which will be fitted to observed electron densities, for which a wealth of data exists. The temperature is then in principle determined by the pressure balance in the momentum equations.

This procedure has been used, e.g., by Munro and Jackson (1977) and gives the correct temperature profile, provided our momentum equations are complete.

3. Equations for Minor Ion Charge States

The continuity equation which describes the evolution of charge states of a minor species is

$$\frac{\mathrm{d}n_i}{\mathrm{d}t} = n_e(q_{i-1}n_{i-1} - \alpha_{i-1}n_i - q_i n_i + \alpha_i n_{i+1}) . \tag{3}$$

($i = 0, \ldots, Z$; n_i, density of charge state X^{i+}; q_i, ionization rate from X^{i+} to $X^{(i+1)+}$; α_i, recombination rate from $X^{(i+1)+}$ to X^{i+}; Z, atomic number of the species in question.) For the case $i = 0$ (neutral), respectively $i = Z$ (fully ionized), the first, respectively the last two terms of the right-hand side of Equation (3), have to be omitted.

For a stationary flow in the flux tube geometry described above, Equation (3) can be transformed into a more convenient form by introducing dimensionless fluxes

$$y_i = \frac{n_i u_i}{\sum_i n_i u_i} \tag{4}$$

and with our assumption of equal velocity u for all charge states of one species Equation

(3) becomes

$$u\frac{dy_i}{dr} = n_e[q_{i-1}y_{i-1} - (\alpha_{i-1} + q_i)y_i + \alpha_i y_{i+1}]. \tag{5}$$

In the limit $u \to 0$ the equilibrium of charge states is given by

$$\frac{y_{i+1}}{y_i} = \frac{q_i}{\alpha_i}, \tag{6}$$

whereas for $n_e \to 0$ the charge states become frozen-in:

$$\frac{dy_i}{dr} \to 0, \qquad y_i \to \text{const.} \tag{7}$$

The values of the ionization and recombination coefficients q_i and α_i as functions of (electron-) temperature are taken from Shull and Van Steenberg (1982).

H and He can always be assumed to be fully ionized in the range of temperatures and densities considered, so that charge state calculations only apply to minor ions heavier than helium.

To calculate minor ion charge states, we thus need to know n_e and T (contained in q_i and α_i) as well as the minor ion velocity u, which in turn depends on n, T, and U of the major components.

4. Equations for a Proton-Electron Model

For simplicity, we first present a one-fluid model in which α-particles are treated as minor ions. The equations for the main gas (with $T_p = T_e = T$) are then:

$$n_p = n_e = N \qquad \text{(charge neutrality)}, \tag{8}$$

$$u_p = u_e = U \qquad \text{(zero current)}, \tag{9}$$

$$\frac{1}{a}\frac{d}{dr}(aNU) = 0 \quad \text{(continuity)}, \tag{10}$$

and

$$mNU\frac{dU}{dr} = -\frac{dP}{dr} - \frac{GMmN}{r^2} - \frac{dP_w}{dr} \quad \text{(momentum)}. \tag{11}$$

(n_p, n_e, u_p, u_e, density and radial velocity of protons and electrons; P, pressure of p–e gas; G, gravitational constant; M, solar mass; m, proton mass; r, radial distance from the Sun; P_w, wave pressure.)

Equation (10) has the integral

$$aNU = F = \text{const.} \tag{12}$$

By specifying a flux tube geometry $a(r)$, a density profile $N(r)$ – obtained from

measured electron densities – and the flux F, the velocity $U(r)$ as well as $\mathrm{d}U/\mathrm{d}r$ can be calculated. Inserting this, and

$$P = 2NkT,$$

into Equation (11) yields a differential equation for the temperature:

$$\frac{\mathrm{d}T}{\mathrm{d}r} + T\frac{1}{N}\frac{\mathrm{d}N}{\mathrm{d}r} = -\frac{m}{2k}U\frac{\mathrm{d}U}{\mathrm{d}r} - \frac{GMm}{2kr^2} - \frac{1}{2Nk}\frac{\mathrm{d}P_w}{\mathrm{d}r}. \tag{13}$$

An expression for the wave pressure as a function of U (but not T) will be given below.

Setting

$$T \to 0 \quad (r \to \infty) \tag{14}$$

as a boundary condition, Equation (13) is integrated to give $T(r)$. The integration is simplified by choosing $x = R_\odot/r$ as independent variable. The infinite interval $[R_\odot, \infty)$ in r then transforms into $[0, 1]$ in x.

4.1. Wave pressure

For the wave pressure we use an expression for nonresonant, undamped Alfvén-waves in the WKB-approximation (cf. Dewar, 1970; Belcher, 1971; Alazraki and Couturier, 1971; Hollweg, 1974). The wave pressure is

$$P_w = \frac{\delta B^2}{8\pi}, \tag{15}$$

where δB is the fluctuating part of the magnetic field. Conservation of wave action implies (cf. Hollweg, 1974; Jacques, 1977)

$$\frac{(U + V_A)^2 a\, \delta B^2}{V_A} = \text{const.}, \tag{16}$$

where V_A is the radial Alfvén speed

$$V_A = \frac{B_r}{\sqrt{4\pi\rho}}. \tag{17}$$

At the coronal base we have $U \ll V_A$, thus

$$V_A a\, \delta B^2 = \text{const.} = 4\pi f_{w0}, \tag{18}$$

where f_{w0} is the wave energy flux entering the corona from below. The acceleration due to waves,

$$\mathbf{a}_w = \frac{1}{mN}\nabla P_w, \tag{19}$$

is then given by

$$\mathbf{a}_w = \frac{f_{w0}}{4mF} \frac{(3U + V_A)UV_A}{(U + V_A)^3} \left(\frac{1}{U} \frac{dU}{dr} + \frac{1}{a} \frac{da}{dr} \right) \mathbf{e}_r . \tag{20}$$

4.2. Parametrization of the density profile

We parametrize observed electron density profiles by

$$N(x) = \sum_j c_j x^{b_j}, \qquad x = \frac{R_\odot}{r}, \tag{21}$$

where the b_j are positive, but not necessarily integer. Writing $b_{\min}$ for the minimum value of the b_j, it can be shown (for $P_w = 0$) that T diverges asymptotically for $x \to 0$ if $b_{\min} > 2$. On the other hand, $b_{\min} < 2$ gives a decreasing velocity for $r \to \infty$. Thus we will always take $b_{\min} = 2$. The other remaining exponents b_j are chosen such that a given set of electron density data can be well approximated with a minimum of terms in the sum, and generally such that all coefficients c_j are positive (to avoid oscillations). The c_j are determined by a least-squares fit to a set of data points.

Since coronal electron density observations are usually restricted to $r < 5$–$10\ R_\odot$, the coefficients of the lowest powers of x (usually x^2 and x^3) in the sum (21) are not well determined by the fit. The extrapolation of the density profile to infinity can be made unique, however, by also prescribing the density at 1 AU (n_{AU}), together with the fact that $n_e \sim x^2$ for $x \to 0$ ($r \to \infty$) as discussed above.

A model is thus determined by:

- the choice of a geometry $a(r)$ (parameters f_m, r_1, σ_1);
- a coronal electron density model given by a set of data points and n_{AU};
- the particle flux F;
- specification of P_w (parameters f_{w0} and B_0).

Having chosen $a(r)$ and a set of coronal electron density data, and neglecting P_w in the case of the low-speed solar wind, the remaining free parameters are n_{AU} and F. These two parameters influence mainly the model-properties at large distances, and they are chosen such that the observational values of the solar wind properties at 1 AU are matched, i.e.,

$$U_{AU} \simeq 300 - 400 \text{ km s}^{-1}, \qquad T_{AU} \simeq 10^5 \text{ K} \quad (\simeq (T_p + T_e)/2)$$

for the low-speed solar wind.

5. Momentum Equation for Minor Ions

The momentum equation for minor ions contains terms additional to those in the equations for the main gas, describing interactions between major and minor ions. These additional terms are:

- an electric force due to the charge separation electric field;
- momentum transfer between the main gas and the minor ions in the form of:

(a) friction, if the velocities of major and minor ions differ, and

(b) heat flow interactions in the collision term, which cause a thermal force if the distribution functions are asymmetric due to the presence of temperature gradients (thermal diffusion);

– rotational forces, caused by the nonradial magnetic field in the solar wind, and

– momentum transfer between charge states due to ionization/recombination. (This does not enter into the equations in the case studied here, since we assume the velocities of all charge states of one species to be equal.)

The equation of motion for an ion of mass $Am = Am_p$, charge $Z_x e$, density n_x, velocity u, partial pressure $p_x = n_x kT$ is then

$$Amn_x(\mathbf{u}\cdot\nabla)\mathbf{u} = -\nabla p_x - \frac{GMAmn_x}{r^2}\mathbf{e}_r + Z_x e n_x \mathbf{E}^* + \\ + \mathbf{F}_c + \mathbf{F}_t + \mathbf{F}_r + \mathbf{F}_w, \tag{22}$$

where $\mathbf{E}^*$ is the effective electric field,

$$\mathbf{E}^* = \mathbf{E} + \frac{\mathbf{u} - \mathbf{U}}{c} \times \mathbf{B},$$

$\mathbf{F}_c$ the force density due to Coulomb friction, $\mathbf{F}_t$ the thermal force density, $\mathbf{F}_r$ the rotational force density and $\mathbf{F}_w$ the wave force density.

For the electric field $\mathbf{E}$ we take the charge separation electric field obtained from the electron momentum equation by taking the limit $m_e \to 0$:

$$e\mathbf{E} = -\frac{1}{n_e}\nabla p_e. \tag{23}$$

An additional electric field caused by the thermal force on electrons, which enters Equation (23), will be taken into account in the thermal diffusion coefficients of ions.

Coulomb friction with protons is given by

$$\mathbf{F}_c = \frac{4\pi e^4 \ln(\Lambda)}{kT} n_p Z_x^2 \frac{\Delta\mathbf{u}_{xp}}{|\Delta u_{xp}|} G(X_{xp}), \tag{24}$$

with

$$X_{xi} = \left(\frac{\mu_{xi}}{2kT}\right)^{1/2} |\Delta u_{xi}|, \qquad \Delta\mathbf{u}_{xi} = \mathbf{U}_i - \mathbf{u}_x, \tag{25}$$

$$G(X) = \frac{\mathrm{erf}(X) - X\,\mathrm{erf}'(X)}{2X^2} \tag{26}$$

(cf. Burgers, 1969). For the Coulomb logarithm, we take the constant value $\ln(\Lambda) = 21$.

The thermal force, caused by heat flow interactions, is

$$\mathbf{F}_t = \sum_i \nu_{xi} \frac{3\mu_{xi}}{5kT}\left[\mathbf{q}_x - \frac{\rho_x}{\rho_i}\mathbf{q}_i\right] H(X_{xi}), \tag{27}$$

$$H(X) = (1 - 2X^2)\, e^{-X^2}, \tag{28}$$

see Burgers (1969) and Salat (1975) for the velocity dependent part $H(X)$. ν_{xp} is the Coulomb collision frequency (cf. Schunk, 1975), the summation is over $i = p, e$ (all main gases, in general), μ_{xi} is the reduced mass and ρ the mass density of the species in question.

In what follows, we will use the expressions for the heat fluxes in a collision dominated plasma. Since the thermal force will later turn out to be important near the coronal base only (mainly due to the strong velocity cutoff in Equation (28)), this should be a reasonable approximation. In a collision dominated plasma, the heat fluxes can readily be calculated, and are proportional to the temperature gradient (cf. St. Maurice and Schunk, 1977). For electrons the argument of the function $H(X_{xe})$ is always very small and, hence, $H(X_{xe})$ always very close to unity. There results

$$\mathbf{F}_t = n_x k(\alpha_{xp} H(X_{xp}) + \alpha_{xe}) \frac{\mathrm{d}T}{\mathrm{d}r} \cos\varphi\, \mathbf{e}_1\,; \tag{29}$$

α_{xp} and α_{xe} are the well-known thermal diffusion coefficients,

$$\alpha_{xp} = \frac{15\sqrt{2}}{8}\left(\frac{A}{A+1}\right)^{3/2} Z_x^2\left[1 - \frac{27}{30A^2 + 16A + 13}\right] - \frac{15(A+1)}{30A^2 + 16A + 13}, \tag{30}$$

$$\alpha_{xe} = \frac{15\sqrt{2}}{13\sqrt{2} + 8}(Z_x^2 - Z_x), \tag{31}$$

for the case at hand (see Schunk and Walker, 1969; St. Maurice and Schunk, 1977).

The term proportional to $-Z_x$ in (31) takes into account the electric field caused by the thermal force on electrons, which has been neglected in (23), $\mathbf{e}_1$ is a unit vector pointing in the direction of the magnetic field, φ is the angle between the radial direction and the magnetic field. In deriving Equations (27), (28), and (29) we have taken into account the fact that in the solar wind all heat fluxes and velocity differences are always parallel (or antiparallel) to the magnetic field.

We have also neglected the (small) contribution of speed differences to the heat fluxes, which would result in a correction factor of the drag term. There remains, however, the question whether the heat fluxes derived for a collision dominated plasma really apply (cf. Hollweg, 1976; Ogilvie and Scudder, 1978; Feldman *et al.*, 1979; Scudder and Olbert, 1979a, b; Cuperman *et al.*, 1980, 1981b). As of today, there is no generally accepted formulation for the collisionless heat fluxes (partly for this reason we have avoided to use the energy equations, cf. Section 2), so we use the collisional heat fluxes,

but introduce an *ad hoc* cut-off factor

$$f_c = e^{-(\lambda_{ee}/H_t)^2} \tag{32}$$

into Equation (29) (λ_{ee}, mean free path of electrons between collisions, Spitzer, 1956; H_t, temperature scale-height), which is $\simeq 1$ when $\lambda_{ee} \ll H_t$ and prevents the thermal force from being excessively large when the (smaller) collisionless heat fluxes apply. Although an exact treatment of collisionless heat fluxes would be highly desirable, even more so with regard to the energetics of the solar wind, it would not qualitatively change the results presented in this study as far as the thermal force is concerned, since besides the factor (32), the velocity dependence of the thermal force (Equation (28)) provides a very strong cut-off in the trans- and supersonic regions as well.

The rotational forces are produced by solar rotation, which winds up the magnetic field into a spiral (at large r). We take into account the magnetic and inertial forces (from $(\mathbf{u} - \mathbf{U}) \times \mathbf{B}$ and $(\mathbf{u} \cdot \nabla)\mathbf{u}$) as worked out by McKenzie *et al.* (1979). The only difference to their momentum equation is, that we have included the thermal force, and that we insert $\Omega = \Omega(r)$ for the relative angular velocity of the Sun as seen from the local eigensystem of the solar wind (so that $\Omega(r \to \infty) \to \Omega_0 = \text{const.}$). The radial acceleration due to rotational forces results as

$$\frac{w^2}{r} + \frac{\Omega r}{U} \frac{\mathrm{d}}{\mathrm{d}r}(wr), \qquad w = \frac{\Omega r}{U}(U - u), \tag{33}$$

w is the azimuthal component of the minor ion velocity, U and u are the radial velocity components of the main and minor species, and $\Omega(r)$ is given by (Weber and Davis, 1967)

$$\Omega(r) = \frac{(1 - r_A^2/r^2)}{(1 - V_A^2/U^2)} \sin \vartheta, \tag{34}$$

(r_A, Alfvén-radius). Compared to the radial case, we also have an additional factor

$$1 + \frac{\Omega^2 r^2}{U^2} = \frac{1}{\cos^2 \varphi},$$

by which the radial components of the drag and thermal forces are multiplied.

It should be noted that what we call 'rotational forces' does not include the centrifugal force, in order not to introduce an extra singularity (at $r = r_A$) into the main gas equations. The term $\mathbf{F}_r$ in Equation (22) is in fact zero, and written only for a symbolic reason, since all the rotational forces arise from the inertial and magnetic terms.

The wave forces for Alfvén waves (as specified in Section 4.1) have also been calculated by McKenzie *et al.* (1979). Their result for the (nonresonant) acceleration is

$$\mathbf{a}_w = \tfrac{1}{2} \frac{\mathrm{d}}{\mathrm{d}r} \left[\frac{\delta B^2}{B_r^2} [(U + V_A)^2 - u^2] \right] \mathbf{e}_r, \tag{35}$$

which becomes equal to (20) for the proton main gas. B_r is the radial component of the magnetic field,

$$B_r(r) = \frac{B_0}{a(r)}. \tag{36}$$

The equation of motion can now be written for each charge state. By summing up the equations for the charge states of a given species, using the assumption of equal velocity, and introducing the mean values

$$Z = \frac{\Sigma n_x(r) Z_x}{\Sigma n_x(r)}, \qquad Z^2 = \frac{\Sigma n_x(r) Z_x^2}{\Sigma n_x(r)}, \tag{37}$$

the radial equation of motion for minor ions then finally becomes

$$\begin{aligned}
&\frac{1}{u}\frac{\mathrm{d}u}{\mathrm{d}r}\left[u^2\left(1+\frac{\Omega^2 r^2}{U^2}+\frac{4\pi f_{w0} a V_A}{B_0^2 (U+V_A)^2}\right)-\frac{kT}{Am}\right] = \\
&= \frac{k}{Am}\frac{\mathrm{d}T}{\mathrm{d}r}+\frac{kT}{Am}\frac{1}{a}\frac{\mathrm{d}a}{\mathrm{d}r}-\frac{GM}{r^2}+\frac{Ze}{Am}E_r + \\
&+\frac{1}{\cos\varphi}\frac{4\pi e^4 \ln(\Lambda) n_p}{mkT}\frac{Z^2}{A}G(X_{xp}) + \\
&+\frac{k}{Am}\left[\alpha_{xp}H(X_{xp})+\alpha_{xe}\right]\frac{\mathrm{d}T}{\mathrm{d}r}f_c + \\
&+\frac{\Omega^2 r^2}{U^2}\left[\frac{U^2-u^2}{r}+u(U-u)\frac{1}{\Omega}\frac{\mathrm{d}\Omega}{\mathrm{d}r}+\frac{u^2}{U}\frac{\mathrm{d}U}{\mathrm{d}r}\right] + \\
&+\frac{\pi f_{w0} a V_A}{B_0^2}\left[\frac{1}{U}\frac{\mathrm{d}U}{\mathrm{d}r}\left(1+\frac{(3U+V_A)}{(U+V_A)^3}u^2\right)+\right. \\
&\left.+\frac{1}{a}\frac{\mathrm{d}a}{\mathrm{d}r}\left(1-\frac{(U+3V_A)}{(U+V_A)^2}u^2\right)\right].
\end{aligned} \tag{38}$$

We have expanded the derivatives in Equations (33) and (35), since the complete momentum equation has to be solved numerically.

The procedure for numerical integration is iterative: to start, we assume $u(r) = U(r)$, solve (5) for the charge states $y_i(r)$, then use these solutions to calculate $Z(r)$, $Z^2(r)$ which are used to get a new $u(r)$. The two steps are repeated until the solutions have sufficiently converged to $\delta u/u < 10^{-4}$, which is usually the case after 3–4 iterations.

A method developed by Beutler (1979) is used for all numerical integrations, its details are described by Bürgi (1984).

6. Low-Speed Solar Wind: Results for the One-Fluid Model

Our aim is to present a model for the low-speed solar wind, i.e., with $U(1\text{ AU}) = 300\text{–}400\text{ km s}^{-1}$ and $T(1\text{ AU}) \simeq 10^5\text{ K}$, using the procedure described in Sections 2 and 4.

For the first set of models (Model 1, 1A–1D), we use the n_e-data obtained by Saito (1970) for the quiet equatorial corona at solar minimum. For the basic model (Model 1) we take $n_{\text{AU}} = 10\text{ cm}^{-3}$. We also fit two other sets of coefficients to the same coronal densities using $n_{\text{AU}} = 8$, respectively, 12 cm^{-3} (Models 1A and 1B). The resulting density profiles are shown in the top panel of Figure 1(a). Next we decide to use a simple radial geometry, neglect wave pressure, and determine the particle flux by requiring that the velocity at 1 AU be 360 km s^{-1}. For comparison, we also calculate models with $U(1\text{ AU}) = 330$ and 390 km s^{-1} (Models 1C and 1D), using the density fit of Model 1.

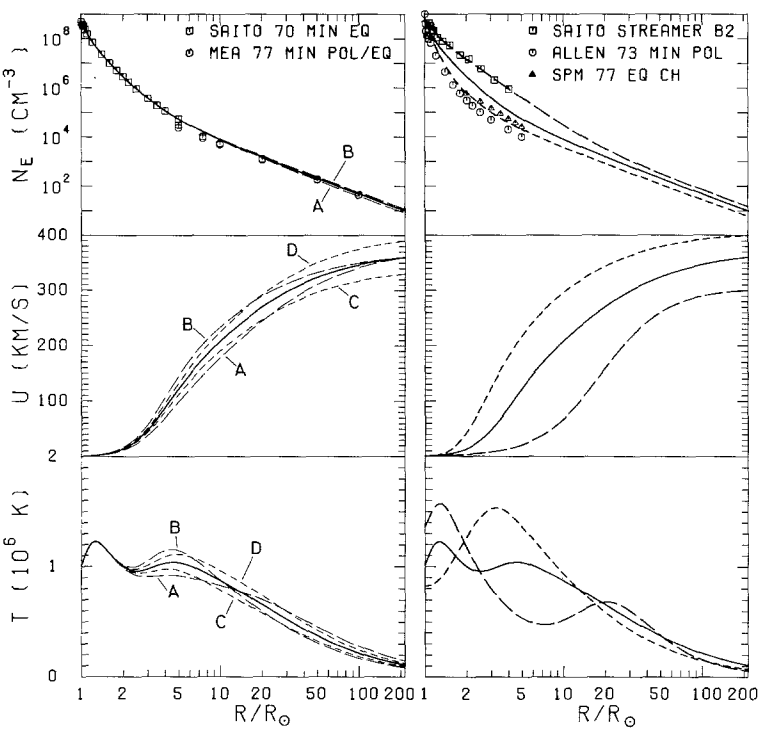

Fig. 1a. Fig. 1b.

Fig. 1(a–b). (a) The one-fluid (p–e gas) model for the equatorial background corona. Solid line: Model 1; broken lines: variations of boundary conditions at 1 AU (Models 1A–1D). The adopted n_e profile is a fit to the data points of Saito (1970). Also shown are data points (MEA 77) that were calculated from an analytical fit given by Muhleman *et al.* (1977). These data are for the equator only for $r > 10\,R_\odot$, where they agree well with our extrapolation. (b) Comparison of one fluid models for the minimum corona (Model 1, solid line), a coronal streamer (Model 2, long dashes), and a coronal hole (Model 3, short dashes). Data points are for streamer B_2 of Saito (1972), the polar corona at solar minimum (Allen, 1973), and an equatorial coronal hole (Saito *et al.*, 1977, SPM 77).

The parameters of these, and models described below are summarized in Table VII at the end of the paper.

The temperature profiles resulting from Equation (13) are shown in the bottom panel of Figure 1(a). The main features are the following: below $r \simeq 2\,R_\odot$ the model temperature is insensitive to our choice of parameters. The maximum temperature (at $1.25\,R_\odot$) is only 1.23×10^6 K. This can easily be understood from Equation (13): in the subsonic region we have

$$U^2 \ll \frac{2kT}{m}$$

and also, since except in the transition region the temperature varies much more slowly than the density,

$$\frac{1}{T}\frac{\mathrm{d}T}{\mathrm{d}r} \ll \frac{1}{N}\frac{\mathrm{d}N}{\mathrm{d}r}.$$

Equation (13), therefore, reduces to an algebraic equation for T:

$$T \simeq -\frac{GMm}{2kr^2}\left(\frac{1}{N}\frac{\mathrm{d}N}{\mathrm{d}r}\right)^{-1}. \tag{39}$$

The temperature (in the subsonic region) is thus entirely determined by the slope of the density, and is insensitive to the choice of our free parameters n_{AU} and F, as well as to the geometry of the subsonic region (although the extent of the latter region is of course affected by these parameters).

In the trans- and supersonic region, the temperature increases when $U(1\ \mathrm{AU})$ is increased, which is to be expected in a thermally driven model. Increasing n_{AU}, on the other hand, decreases the temperature at 1 AU.

A probably artificial feature of all profiles is the existence of a secondary temperature maximum near $r = 4$–$5\,R_\odot$, i.e. in the main acceleration region of these models (cf. the middle panel of Figure 1(a)). This feature gets more pronounced, with increasing n_{AU} or $U(1\ \mathrm{AU})$, i.e., increasing flux F. Structures with two temperature peaks have also been found by Sittler (1978) in a similar model. These secondary peaks always appear in the region where we have extrapolated the n_e-data. Since our aim is mainly to model the inner corona, we shall not be concerned about the physical significance of these secondary peaks.

Regardless of the choice of the boundary conditions, we obtain maximum temperatures much lower than coronal temperatures inferred from spectroscopic and solar wind charge-state measurements. Table I summarizes some of these determinations: it can be seen that the freezing-in temperature of oxygen (O^{6+}/O^{7+}) should be around $T_f = 1.6$–1.8×10^6 K, which is a well determined average, but from our model we cannot expect a freezing-in temperature which is higher than the maximum temperature. In fact the solution for velocity and charge states of oxygen in Model 1 gives

TABLE I

Determinations of coronal temperatures

Authors	$T/10^6$ K	Remarks	Method
Fort *et al.* (1972)	1.95	T_{max} at $r = 1.23\ R_\odot$	Fe XIV green line
Bame *et al.* (1974)	1.7–2.5	T_{max} at $R_\odot$	Freezing-in temperatures
	1.84 ± 0.13	mean value	of O, Si, Fe
Ogilvie and Vogt (1980)	1.6 ± 0.2	Low speed S.W., mean value	Freezing-in temperature O^{6+}/O^{7+}
Withbroe *et al.* (1982)	2.6	$r = 1.5\ R_\odot$	H Lα Doppler width
	1.2	$r = 4\ R_\odot$	
Kunz *et al.* (1983)	2.13–2.45	Three selected periods, low speed S.W.	Freezing-in temperatures
	1.94–2.12		
	1.66–1.75		
Bochsler (1984)	1–2.5		Freezing-in temperature
	1.7	Mean value	O^{6+}/O^{7+}

$T_f(O^{6+}/O^{7+}) = 1.13 \times 10^6$ K only. The radial evolution of carbon and oxygen charge states in Model 1 is shown in Figure 2. It can be seen that the charge states remain near equilibrium around the temperature maximum and freeze in only at $\simeq 1.5\ R_\odot$.

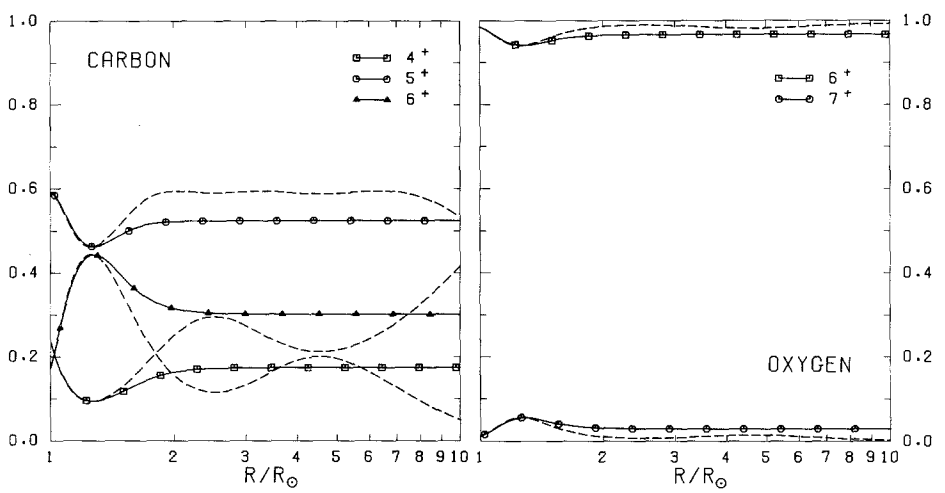

Fig. 2. Development of charge states of carbon and oxygen in Model 1 (minimum corona, one fluid). Dashed lines correspond to equilibrium values at local temperature. The low temperature of Model 1 gives charges that are significantly lower than those usually observed in the low speed solar wind.

Since our first model turns out to be unrealistic, we have to find out whether the reason for this is incomplete physics, or whether it is the wrong choice of the density model for the source region of the low speed solar wind.

We will first explore the second possibility. Figure 3 shows several sets of coronal electron densities. Three groups can clearly be distinguished: (a) the quiet background

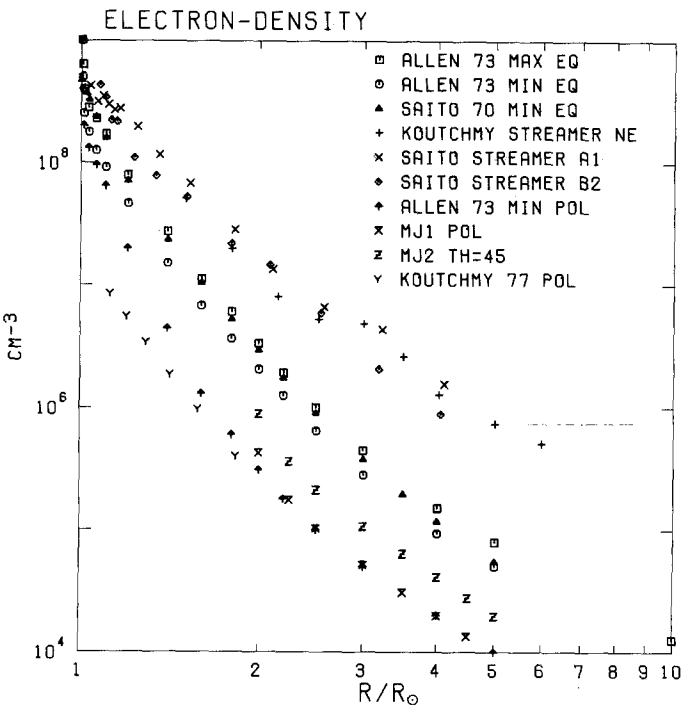

Fig. 3. Comparison of measured electron densities for the background corona, coronal streamers, and coronal holes. Some of the 'data points' have been calculated from analytical expressions given by the respective authors. Data are for the equatorial background corona at solar maximum (Allen, 1973), the equatorial background corona at solar minimum (Allen, 1973, Saito, 1970), three different coronal streamers (Koutchmy, 1972; Saito, 1972), the polar corona at solar minimum (Allen, 1973), the polar coronal hole (MJ1) and its extension to $\vartheta = 45°$ (MJ2) by Munro and Jackson (1977), and the polar coronal hole of Koutchmy (1977).

corona with average densities, (b) coronal streamers, and (c) coronal holes. The latter two have densities which are about an order of magnitude larger (b) or smaller (c) than the quiet background. For both streamers and coronal holes the n_e-profiles seem to be flatter than for the background corona, which indicates a higher coronal temperature (see Equation (39)).

Coronal holes are associated with high speed solar wind (cf. Krieger *et al.*, 1973; Nolte *et al.*, 1976; Sheeley *et al.*, 1976; Bame *et al.*, 1977) whereas the signature of streamers in the solar wind is low speed, very high density, unusually low n_α/n_p, and association with reversals of the magnetic field (Borrini *et al.*, 1981; Gosling *et al.*, 1981). Furthermore, both types of structures deviate significantly from radial geometry. Since the average low speed solar wind could originate in the surroundings of either coronal holes or streamers, where the nonradiality is less pronounced, but the density is still significantly different from the average quiet corona, we fit a profile to one representative of each group, and use a simple radial geometry to facilitate comparison with Model 1.

Model 2 is fitted to the density of streamer B_2 from Saito (1972), the streamer nearest to the equator in that work. To extrapolate the high densities to large distances, we

choose a relatively high n_{AU} of 15 cm^{-1}, and a low U_{AU} of 300 km s^{-1}, in order not to get an excessively high secondary temperature peak. The profiles for $N(r)$, $U(r)$, and $T(r)$ in Model 2 are shown in Figure 1(b). The maximum temperature is in fact higher (1.57×10^6 K) than in Model 1, but is still too low compared to the observed freezing-in temperatures at 1 AU. The situation for charge states has not even improved, as Figure 4 shows for C and O: the temperature maximum is very near to the Sun, and the temperature falls off rapidly beyond (a feature which is insensitive to boundary conditions). Due to the high densities the charge states freeze-in at larger distances than in Model 1, i.e., at even lower temperatures, leading to a freezing-in temperature of only 0.99×10^6 K for O^{6+}/O^{7+}.

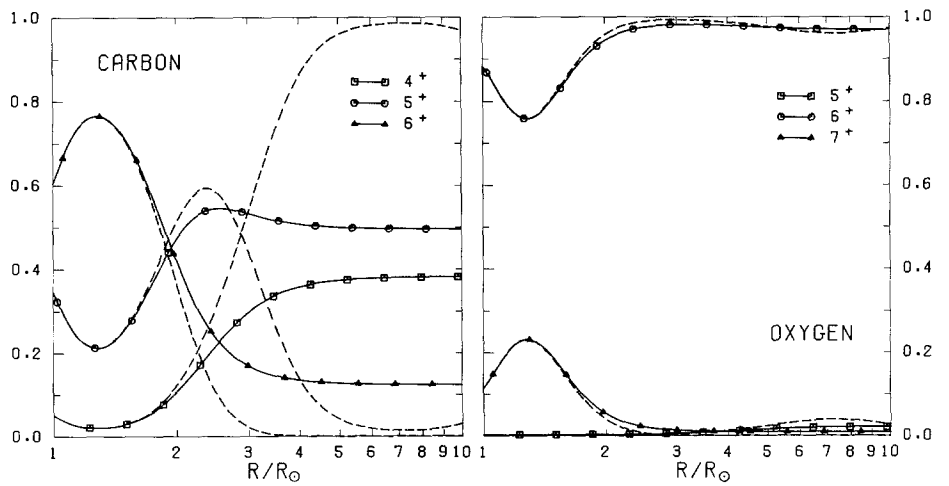

Fig. 4. Charge states of carbon and oxygen in Model 2 (streamer). Due to the high density and steep temperature gradient of this model the equilibrium (dashed lines) is followed out to low temperatures, and frozen-in charges are again too low compared to observations.

Model 3 is fitted to the data for the polar coronal hole of Allen (1973), which covers the largest radial range of the available coronal hole data. Since equatorial coronal holes are about twice as dense as polar ones (Saito *et al.*, 1977), we have then doubled the n_e-fit obtained. Parameters of Model 3 are $n_{AU} = 6$ cm^{-3} and $U_{AU} = 400$ km s^{-1}, the resulting profiles are included in Figure 1(b). The maximum temperature (1.54×10^6 K) is again higher than in Model 1, but it is reached quite far from the Sun (at 3.2 $R_\odot$). This, together with the low density, is again problematic for minor ions: the proton drag, which goes roughly as

$$n_p U T^{-3/2}, \tag{40}$$

is very small near the temperature maximum. The upper panel of Figure 5 shows the topology of the solutions for the velocity of O^{6+}. There are three critical points, and the solution goes through the outermost one. The steady state velocity in the corona is

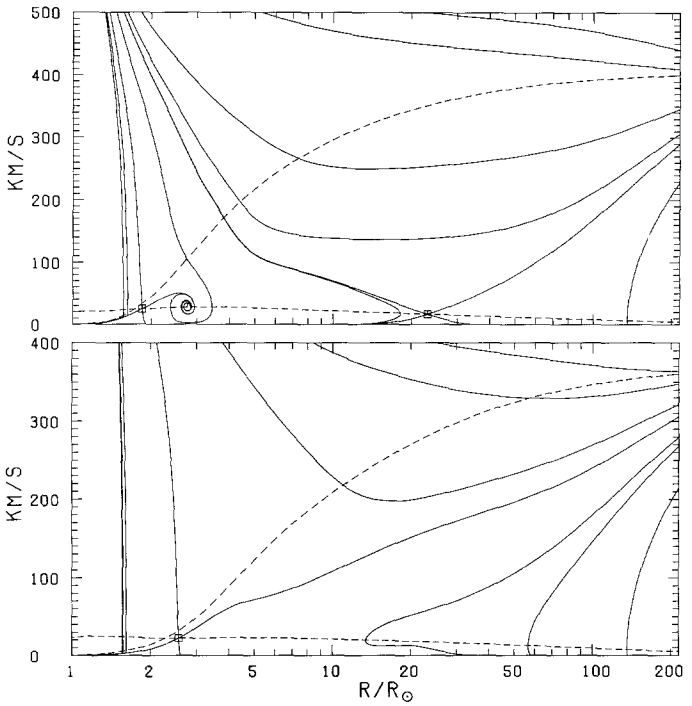

Fig. 5. Solution topology for the velocity of the ion O^{6+} (with fixed charge) in the coronal hole Model 3 (upper panel) and in Model 1 (lower panel). In the coronal hole case there are three critical points, and the solution goes through the outermost one. This solution has such low velocity in the lower corona, however, that the time required to build up the steady state is far longer than the lifetime of coronal structures. There is no such problem in Model 1 (lower panel), where the solution goes through a critical point near the Sun, even though two additional critical points which have not been resolved may exist in the region 15–20 $R_\odot$. Dashed lines correspond to the proton speed and to the critical velocity for which the left-hand side of Equation (38) becomes zero.

practically zero, so that we have to interpret this as the absence of oxygen from the solar wind, because a solution of this type would require far longer times to reach steady state than times over which coronal features exist. The situation might be changed if there were another force contributing to the acceleration of oxygen near $r \simeq 3$–$5\ R_\odot$, e.g., waves. But waves would also contribute to the pressure, and since we derive the model temperature from the pressure balance, the presence of waves would again lower the model temperature. For comparison, the lower panel of Figure 5 shows the same topology for Model 1, where the solution goes through a critical point near the Sun.

Thus we have to reject both Models 2 and 3. Since the exploration of alternative density models has led to no improvement in the reproduction of coronal and oxygen freezing-in temperatures, we now investigate the second plausible cause for this failure, i.e., incomplete physics of our model.

We have to improve either (a) the calculation of charge states, (b) the minor ion dynamics, or (c) the model for the main gas (or all of them).

Regarding (a), an obvious shortcoming of the model is that our ionization and recombination rates are based on Maxwellian electron distributions. As has been shown by Owocki and Scudder (1983), tails in the electron distribution functions would lead to stronger ionization especially of the pair O^{6+}/O^{7+}. These tails, however, are likely to be more pronounced in regions of low density (i.e., coronal holes), and less so in the high density regions from where we suspect the low speed solar wind to originate, where electrons are collision dominated and therefore more nearly Maxwellian.

As regards (b), our assumptions of equal velocities for all charge states of an element might be in error. As has been shown by Owocki (1982) and Owocki *et al.* (1983), this would again influence the frozen-in charge states. We will therefore check the relevance of unequal ion speeds for a particular example.

Under the diffusion approximation (neglecting thermal diffusion) the speed differences can be approximated by

$$U - u_x \sim \frac{2A - Z - 1}{Z^2} \tag{41}$$

(cf. Geiss *et al.*, 1970). In the freezing-in region of Model 1 ($r = 1.5\,R_\odot$) we have the speed u_6 of O^{6+},

$$\frac{u_6}{U} \simeq \frac{u}{U} = 0.583. \tag{42}$$

$u_6 \simeq u$ since we have relative abundances of 95% O^{6+} and only 4.5% O^{7+}. Evaluating the speed of O^{7+} (u_7) from Equations (41) and (42) we find

$$\frac{u_7}{u_6} = 1.35.$$

For the case of unequal flow speeds the relation (6) for the frozen-in fluxes would change to

$$\frac{y_{i+1}}{y_i} \simeq \frac{u_{i+1}}{u_i}\,\frac{q_i}{\alpha_i}$$

(cf. Owocki *et al.*, 1983). The ratio of fluxes would therefore be lifted by an estimated 35%, but we would still have less than 6% of O^{7+} compared to the $\simeq 25\%$ required for a freezing-in temperature of 1.7×10^6 K.

Even if the mechanisms of (a) and (b) should be more pronounced (e.g., in regions of low density), there remains still the fact that coronal temperatures derived from spectroscopy (see Table I) are much higher than those resulting from our model.

Therefore, we consider case (c) and look for possibilities of lifting the model temperatures by improving the physics of the main gas. We repeat Equation (39),

$$T \simeq -\frac{GMm}{2kr^2}\left(\frac{1}{N}\,\frac{\mathrm{d}N}{\mathrm{d}r}\right)^{-1} \quad \text{(subsonic region)}.$$

Apart from the density profile, only fundamental constants appear in this equation. An additional force acting on the gas, however, would be equivalent to a change of G (the measure of the retarding force). To increase T, the additional force has to be directed towards the Sun, a requirement which rules out the most popular candidate for an additional force in the solar wind, i.e., momentum transfer from waves propagating away from the Sun. Changing the geometry of the flow tube would not help either, since this only produces additional inertial forces which cannot contribute substantially enough in the subsonic region.

There seems to be just one likely candidate of a retarding force other than gravitation: the friction from α-particles slowing down the p–e main gas (see Noci and Porri, 1983). Up to now we have treated α-particles as minor ions with $n_\alpha = 0$. Evidently we now have to drop this assumption and construct a two-fluid model with $n_\alpha > 0$ for the α–p friction to have an effect on the protons.

We can look at Equation (39) from another viewpoint: the factor $m/2$ is the mean mass per particle in the one-fluid model. Including a finite abundance of α's in the effective mass, we get

$$T \sim \overline{m} = m \frac{1 + 4n_\alpha/n_p}{2 + 3n_\alpha/n_p} . \tag{43}$$

According to this, we need $n_\alpha/n_p \simeq 0.25$ to raise T from 1.25 to 1.8×10^6 K. This is not unrealistic in the corona, where U_α may be much smaller than U_p (see Figure 6) and helium is correspondingly enhanced (in the steady state).

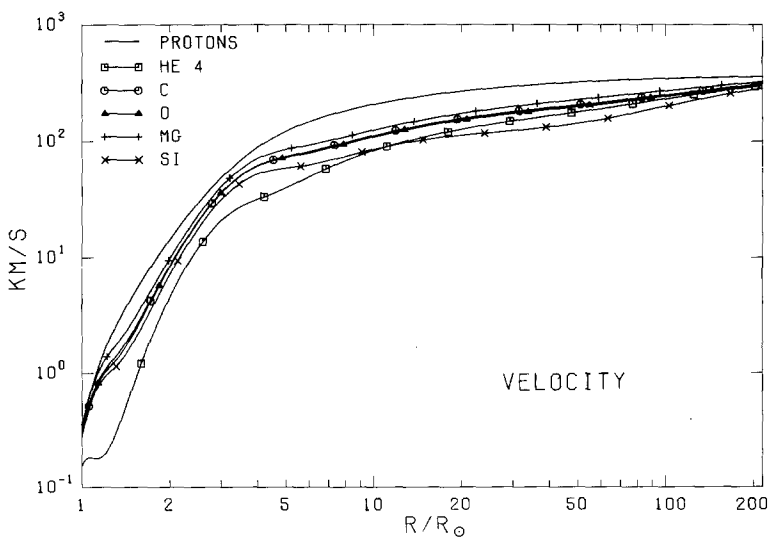

Fig. 6. Velocities for protons, He, C, O, Mg, and Si in the one-fluid Model 1 (minimum corona). In the steady state the large relative lag especially of He behind H implies a corresponding enhancement of density ratios in the corona.

Finally we note that our one-fluid model is not the only one which fails to reproduce high values for both coronal densities and temperatures together with reasonable boundary conditions at 1 AU (i.e., $n_{AU} \simeq 10\,\mathrm{cm}^{-3}$). Thus, e.g., one finds $T_{max} = 1.75 \times 10^6$ K, but only $N(R_\odot) = 3.85 \times 10^6\,\mathrm{cm}^{-3}$ in the one-fluid model of Cuperman *et al.* (1972), or $T_{max} > 2 \times 10^6$ K but $N(R_\odot) < 2 \times 10^6\,\mathrm{cm}^{-3}$ in the models of Steinolfson and Tandberg-Hansen (1977), and $T_{max} > 2 \times 10^6$ K, $N(R_\odot) < 2 \times 10^7\,\mathrm{cm}^{-3}$ in the two-fluid models of Couturier (1977).

The results of simultaneous calculations of the charge states and velocities of minor ions lead to strong constraints on models for the main gas and point to the inadequacy of the one-fluid approximation.

7. The Two-Fluid Model

The term 'two-fluid model' is not used here in its usual sense, i.e., a p–e model with $T_e \neq T_p$. Instead we use it for a p–α–e gas with equal temperatures, but different speeds for the species, because we solve two momentum equations (for p and α).

7.1. Modification of the Equations for the Two-Fluid Model

The main modification to be made for taking into account a finite abundance of helium is to introduce two additional terms describing the collisions of ions with helium: one for dynamical friction and the other for the interaction with the α-heat flux. Dynamical friction with helium is given by Equations (24) to (26), provided the index p is changed to an index α and Z_x^2 to $4Z_x^2$ in Equation (24). The thermal force is still given by Equation (27), but the summation has now to be over $i = p$, α, and e, and Equation (29) is replaced by

$$\mathbf{F}_t = n_x k[\alpha_{xp} H(X_{xp}) + \alpha_{x\alpha} H(X_{x\alpha}) + \alpha_{xe}] \frac{\mathrm{d}T}{\mathrm{d}r} \cos\varphi\, \mathbf{e}_1 . \tag{44}$$

In the calculation of the heat fluxes for deriving (44) from (27) we use again the procedure outlined by St. Maurice and Schunk (1977) and we neglect all dependencies of the q_i on $U_p - U_\alpha$. This is justified since (a) the main effect of the thermal force is to be found low in the corona, where the diffusion approximation is valid, and (b) at large distances we have $n_\alpha/n_p \ll 1$, so that the correction is again small. Even so, the thermal diffusion coefficients are now complicated functions of n_α/n_p. They were given by Bürgi (1984) and will not be repeated here.

After inserting these two additional terms into Equation (38) we have the momentum equation for the two major as well as the minor ions in the two-fluid model, provided that U is reinterpreted as the bulk velocity of the two main gases and that the total mass density is used in the calculation of V_A. To keep the calculations tractable, however, we still use U and V_A as in the one-fluid model for the wave and rotational forces. These forces are of importance mainly near and beyond the Alfvén point, and as long as $n_\alpha/n_p \ll 1$ in this region the error introduced by this simplification is small.

7.2. Numerical procedure for the two-fluid model

The differential equations to be solved to obtain a solution for the two-fluid model are the two momentum equations for p and α, which we solve for T and U_α. In addition we have a continuity equation for each species and the condition of charge neutrality

$$n_p + 2n_\alpha = n_e, \tag{45}$$

which are used to derive U_p from U_α, F_p, and F_α. The latter,

$$F_\alpha = a(r) n_\alpha U_\alpha, \tag{46}$$

is an additional integration constant of the two-fluid model, and can be prescribed in terms of F_α/F_p. Usually we take the canonical value $F_\alpha/F_p = 0.04$.

The method of solution is again iterative: we start with the one-fluid model for T and U_α and then iterate: solutions for U_α (and U_p) starting at the α-critical point, using T from the previous solution, and solutions for T from the proton equation starting at $x = 0$ ($r = \infty$) using the previously found U_α and U_p.

The iteration is stopped when the solutions have converged to better than 0.5%.

This cycle does not converge for every value of F_α/F_p, however, but generally does so if the maximum n_α/n_p is smaller than unity, which also seems a physically realistic upper limit. The mathematical reason is that the coupled system of the momentum equations has singular points which differ from the pure p- or α-critical points (see Metzler and Dryer, 1978). The problem is illustrated by the hypothetical case of a pure α-solar wind ($n_p/n_\alpha = 0$): the role of the two momentum equations has to be interchanged, i.e., the α-equation solved for T and the p-equation for U_p.

p–e and p–α–e models with the same electron density profiles cannot have equal U_p and F_p simultaneously, since helium also contributes to the electrons. To make models comparable, we use for the proton flux of the two-fluid model

$$F_p = F_{p1}\left(1 - \frac{2F_\alpha}{F_p}\right), \tag{47}$$

where F_{p1} is the proton flux in the corresponding one-fluid model. Corresponding models have then roughly equal proton speeds at 1 AU (cf. Table VII). (U_p would be exactly equal only for $U_\alpha = U_p$ at 1 AU.)

7.3. Nonspherical geometry

We have found it necessary to introduce a nonspherical flux tube geometry for the following reasons:

(1) Since part of the corona is filled with closed magnetic structures, open magnetic structures have to expand superradially near the Sun.

(2) Near the temperature maximum, the ratio U_p/U_α can become very large, particularly in the two-fluid models which have higher temperature and thus less proton friction than the one-fluid models. Unreasonably large values of n_α/n_p around $r(T_{\max})$ can be avoided if the flux tube is superradial in this region, as has been extensively discussed by Joselyn and Holzer (1978).

(3) Given the same boundary conditions at 1 AU, nonspherical geometry increases the velocity at $R_\odot$ from $U_p \simeq 0.33$ km s^{-1} (in Models 1, 1A–1D) to higher values. With $f_m \geqq 3$ (Equation (2)) values $U_p \geqq 1$ km s^{-1} are obtained, which are probably more representative of flow velocities in the low corona.

7.4. Influence of finite He-abundance

We have calculated models corresponding to Model 1 (minimum corona), with the exception of the geometry for which we chose the parameters

$$f_m = 3, \qquad \sigma_1 = 0.3\, R_\odot, \qquad r_1 = 1.0\, R_\odot \tag{48}$$

(cf. Equations (1) and (2)). We have varied the flux ratio F_α/F_p from 0.00 to 0.05 in steps of 0.01. The resulting temperature profiles are shown in Figure 7(a). The temperature in the corona increases with increasing F_α/F_p as expected (cf. Equations (39) and (43)), whereas T at large distances decreases. For $F_\alpha/F_p = 0.04$ the maximum temperature is 2×10^6 K at $r = 1.3\, R_\odot$, so that the chances for obtaining the observed charge state

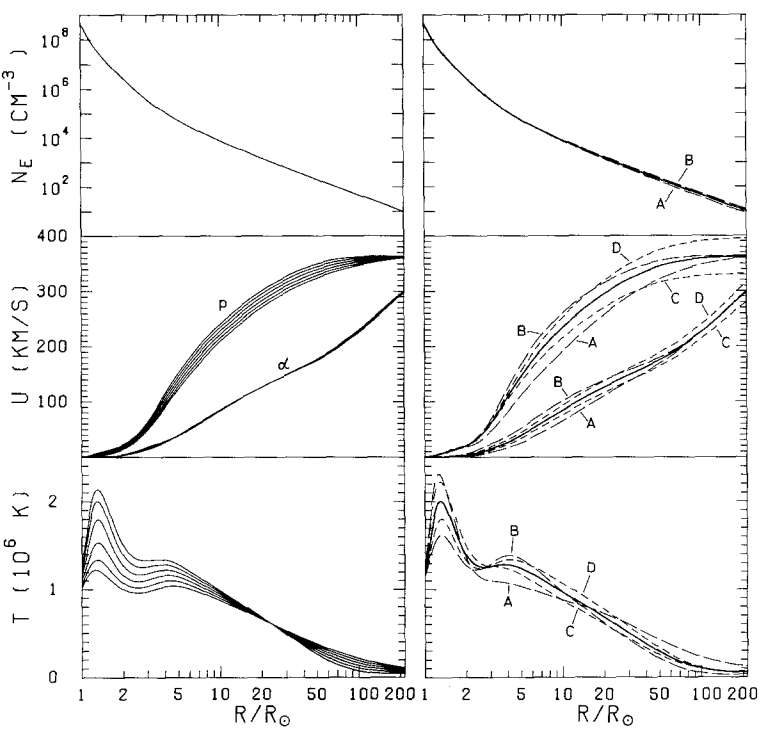

Fig. 7a. Fig. 7b.

Fig. 7(a–b). (a) Influence of finite α-abundance on the main gas model for the minimum corona. The electron density (top) is the same as in Model 1. The ratio F_α/F_p has been varied from 0.00 to 0.05 in steps of 0.01. The proton velocity and the coronal temperature increase with increasing helium flux whereas the temperature at 1 AU decreases. (b) Effect of variation of boundary conditions at 1 AU on Model 4 (minimum corona, $F_\alpha/F_p = 0.04$). Solid line: Model 4, broken lines: Models 4A–4D. For values of parameters see Table VII.

distributions are greatly improved. Another effect of the finite He abundance is that the secondary temperature maximum flattens out with increasing n_α/n_p.

8. The Adopted Two-Fluid Model: Model 4

We now carry out the same variation of parameters U and n_e at 1 AU (cf. Table VII) as for models 1, 1A–1D and call the corresponding two-fluid models 4, 4A–4D. These models all have the geometry given by the parameters (48) and $F_\alpha/F_p = 0.04$, except for Model 4A with $F_\alpha/F_p = 0.02$ only, which already gives $n_\alpha/n_p = 0.72$ at $1.5\,R_\odot$ (cf. Table II).

TABLE II

Helium enhancements and T_{max} in the two-fluid models 4, 4A–4D

$r/R_\odot$	n_α/n_p				
	4	4A	4B	4C	4D
1.0	0.050	0.024	0.048	0.050	0.049
1.2	0.275	0.511	0.092	0.471	0.150
1.5	0.454	0.722	0.185	0.688	0.298
2	0.243	0.263	0.132	0.363	0.179
5	0.151	0.086	0.129	0.162	0.141
10	0.111	0.059	0.103	0.113	0.108
215	0.049	0.024	0.049	0.474	0.050
T_{max} (10^6 K)	2.00	2.31	1.62	2.22	1.80
n_pU_p at 1 AU (10^8 cm^{-2} s^{-1})	3.31	2.76	3.98	3.04	3.59

The results are plotted in Figure 7(b), the values for n_α/n_p are summarized in Table II. Whereas the maximum temperature in the one-fluid model was determined solely by the density profile, there are now large variations is coronal temperature depending on the average atomic mass (cf. Equation (43)) which in turn depends on F_α/F_p and on the proton flux. (The latter determines U_α/U_p and thus n_α/n_p.) From Table II we can see that models with smaller proton flux have indeed higher maximum temperatures. The peak values of n_α/n_p are in the range of 0.2–0.7 (Table II).

Helium enhancements in the corona have been found before in calculations of Geiss *et al.* (1970; implied by their low value of u_α/u_p), by Nakada (1970), and, to an extent depending on the adopted geometry, also by Joselyn and Holzer (1978). Nakada (1970) used a constant temperature and found the largest enhancement of n_α/n_p at $R_\odot$. Using a positive dT/dr near $R_\odot$, which allows for upward thermal diffusion of He and larger drag at low temperature, we find only a moderate enhancement of n_α/n_p at $R_\odot$, but a strong peak near $r(T_{max})$. As has been shown by Joselyn and Holzer (1978), the amount of coronal He-enrichment is also strongly dependent on coronal geometry: forcing the solar wind through a narrow flux tube in the corona can greatly enhance frictional

coupling between H and He and reduce the He-enrichment. We need not repeat their parameter study here, but have chosen a geometry (48) which gives an appreciable, but not excessive He-enhancement (depending on the other parameters) and thus leads to a corresponding increase in the derived coronal temperature, compared to those obtained in the one-fluid models.

The largest values of n_α/n_p (Models 4A and 4C) have limited significance. We have integrated the time needed for ^{4}He-ions to traverse the distance from 1 to 10 $R_\odot$ and found times as long as 28, respectively, 14 days (4A, respectively, 4C), and still 10 days in Model 4. Since the p- and α-velocities in the highly subsonic part are inferred not from the dynamics, but merely from the steady state continuity equation, these large enhancements will take correspondingly long times to build up and might never reach their steady state value, either due to changing conditions in the corona or due to some sort of turbulent mixing.

There is no direct observational evidence for the strong He/H enhancements in certain coronal strata as suggested by our models. However, indirect evidence exists: the solar wind plasma in the driver gas of flare related shocks has high He (up to He/H = 0.3) and Fe contents (Hirshberg *et al.*, 1972; Borrini *et al.*, 1982; Ipavich *et al.*, 1985), and this is interpreted (cf. Hundhausen, 1972) as reflecting an enrichment of the heavier elements in the unperturbed low corona.

This question of a He/H build-up could be clarified by the ensuing direct measurement of He/H as a function of coronal altitude with the Coronal Helium Abundance Experiment on Spacelab 2 (Patchett *et al.*, 1981).

Our two-fluid model shows several features which can be compared to the results for three-fluid p–α–e models, except for our simplification regarding equal temperatures. In fact, our findings are in general agreement with the results of the three-fluid model of Joselyn and Holzer (1978). The main difference between their models and ours is to be found near the coronal base, where we find a positive temperature gradient, lower temperature and higher densities than these authors, and a much smaller enhancement of He/H over the flux-ratio. This is rather a consequence of different procedures than a different result, however, Joselyn and Holzer prescribed a monotonous non-increasing electron temperature, whereas the density profiles we used correspond to an increasing temperature.

The comparison to the three-fluid models of Cuperman and Metzler (1975), Metzler and Dryer (1978), and Cuperman *et al.* (1981a) is more difficult to make: in all these models the transport coefficients have been modified, e.g., the p–α friction coefficient has been increased by a factor of 3. As a consequence of this *ad hoc* increase of frictional coupling, all these authors find much smaller coronal He/H enhancements, in fact one of the main conclusions of Cuperman *et al.* (1981a), i.e., that there are only small differences to be found between models with and without a finite α-abundance is quite opposite to our results. The tendency for the He/H enhancement to be small for strong collisional coupling is also reflected in our model, cf. its dependence on the proton flux discussed above. The approach of the authors quoted above seems to be aimed mainly at modelling the solar wind at large distances and reproducing the solar wind properties

at 1 AU: to obtain this, some modification of the collisional physics has to be allowed for, whereas in the present model, which intends to model the corona and inner solar wind mainly, we think that the no *ad hoc* modification of friction is necessary.

8.1. Minor ions in the two-fluid model: charge states (model 4)

The frozen-in charge state distributions of C, N, O, Ne, Mg, and Si resulting from Model 4 are summarized in Table III. All elements have now much higher charges than in Model 1 (one-fluid). The freezing-in temperature for O^{6+}/O^{7+} is now 1.61×10^6 K, which corresponds well to the observationally determined mean values for the solar wind quoted in Table I. The p–α–e model has thus been successful in reproducing this pair of charge states which is observationally the best determined (due to the relatively large abundance of oxygen), whereas the p–e model has failed to do so.

TABLE III

Frozen-in charge states in the two-fluid Model 4

Ion	Relative abundance	Freezing-in temperature (10^6 K)	Ion	Relative abundance	Freezing-in temperature (10^6 K)
C^{4+}	0.03	1.40	Mg^{8+}	0.03	1.36
C^{5+}	0.24	1.51	Mg^{9+}	0.13	1.41
C^{6+}	0.72		Mg^{10+}	0.82	
N^{5+}	0.27	1.53	Si^{7+}	0.18	1.26
N^{6+}	0.48	1.67	Si^{8+}	0.50	1.22
N^{7+}	0.25		Si^{9+}	0.04	1.61
			Si^{10+}	0.03	1.91
O^{6+}	0.73	1.61	Si^{11+}	0.08	1.85
O^{7+}	0.25		Si^{12+}	0.16	
Ne^{8+}	0.98				

Shown are only ions with relative abundance > 2%. The freezing-in temperatures are for the pairs of ions in the line above and below.

The relative abundances in Table III reflect the stability of ions with closed electron-shells, especially O^{6+}, Ne^{8+}, Mg^{10+}, and Si^{12+}. It can be seen from Table III that the freezing-in temperature varies not only from element to element, but also between ion pairs of the same element (cf. the observations of Zastenker and Yermolaev, 1981). This is especially the case for Si, which has a broad range of charge states with two peaks at Si^{8+} and Si^{12+} with widely different freezing-in temperature. Figure 8 shows the radial development of the relative abundances of charge states of C, O, Mg, and Si together with the equilibrium values corresponding to the local temperature. It can be seen that the charge states follow the local equilibrium fairly well initially, so that the results become independent of the boundary condition imposed at $R_\odot$. The secondary

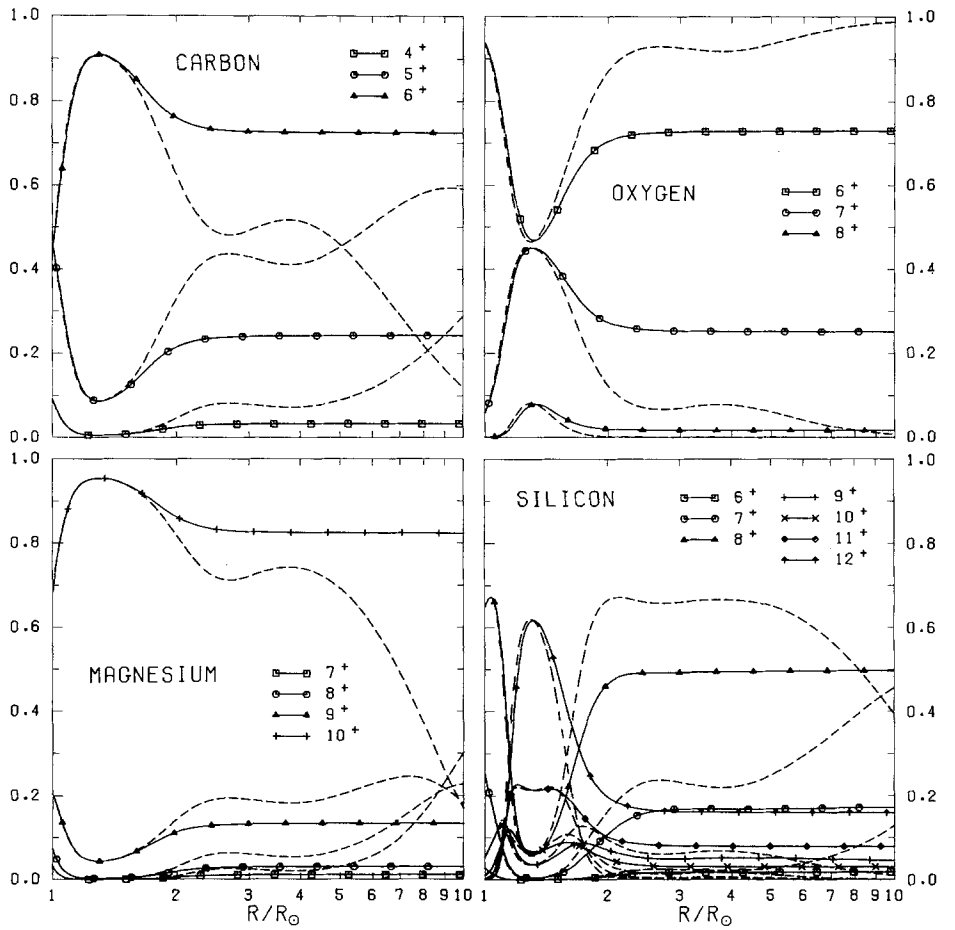

Fig. 8. Solutions for charge states of C, O, Mg, and Si in the two-fluid Model 4. Dashed lines correspond to equilibrium at the local temperature. Note that all ions freeze-in in about the same region, although freezing-in temperatures (Table III) differ considerably.

temperature peak around 4 $R_\odot$ shows up in the equilibrium curves, but hardly influences the charge state distributions which are essentially frozen-in at this solar distance. The case of silicon shows that the freezing-in temperature of a pair of ions sometimes has no correspondence at all to the local temperature in the region where the ions freeze-in: from Table III one might conclude that Si^{11+} and Si^{12+} freeze-in very near the temperature maximum, while a glance at Figure 8 shows that this is not so. The correspondence between freezing-in and local temperature is found in cases such as O^{6+}/O^{7+} where two neighbouring charge states are the dominant ones, but less well when the recombination of the two ions in a pair goes more or less in parallel, as for the pairs Si^{11+}/Si^{12+} or Si^{7+}/Si^{8+}.

8.2. Minor ions in the two-fluid model: velocities (model 4)

The solutions for the velocities of He, C, O, Mg, and Si are plotted in Figure 9: all ions are slower than the protons, which is to be expected since our model contains no force which is able to accelerate them to velocities greater than the proton velocity.

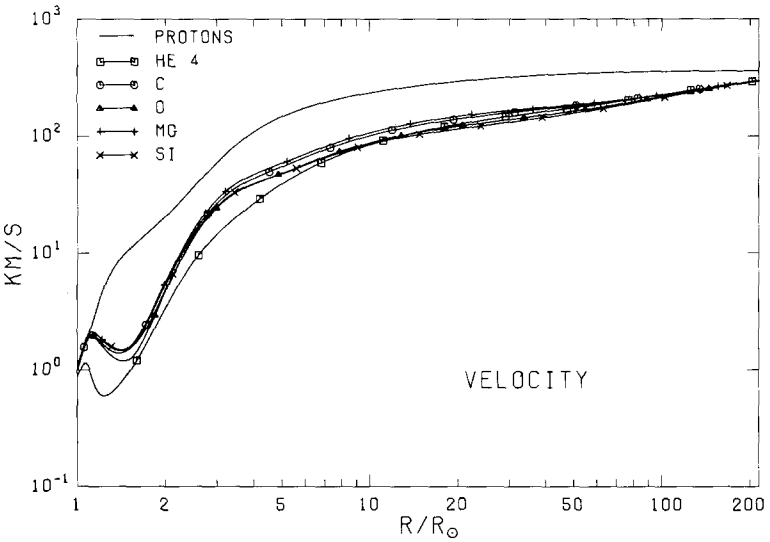

Fig. 9. Solutions for the velocities of H, He, C, O, Mg, and Si in Model 4 (minimum corona, two-fluid).

Observations show that heavy ions travel as fast or faster than protons (Schmidt *et al.*, 1980; Neugebauer, 1981; Marsch *et al.*, 1982a; Ogilvie *et al.*, 1982), the velocity increment is usually somewhat smaller than the local Alfvén speed. This, and the near mass-proportionality of ion temperatures is attributed to some form of resonant wave-particle interaction (cf. Marsch *et al.*, 1982b; Isenberg and Hollweg, 1983). Where exactly this takes place is yet unclear, except that it must be at $r < 70\ R_\odot$ (the Helios perihelion). The theoretical work quoted above indicates that a likely range for the resonant wave-particle interaction to take place is $r = 10$–$40\ R_\odot$ so that our results for smaller r should remain valid.

In Model 4 helium is slower than all minor ions in the range 1–10 $R_\odot$. Comparing the results of Model 4 to those of Model 1 (corresponding one-fluid model) in Figure 6, it can be seen that the introduction of a finite flux of helium leads to a convergence of the minor ion speeds towards the helium speed. Even though the helium drag is an order of magnitude smaller than the proton drag (around $r = 10\ R_\odot$), the helium drag is quite efficient in bundling up the minor ion speeds.

Table IV shows the relative strength of the individual terms in the momentum equations for H, He, and O: while partial pressure and electric field alone accelerate the protons, the relative importance of the pressure decreases as $1/A$ and is almost negligible for oxygen and heavier ions. This would not be the case if temperatures were

TABLE IV

Relative importance of terms in the momentum equation of H, He, and O in Model 4, normalized to gravity

Element	$r/R_\odot$	I	P	G	E	C_p	C_α	T	R
H	1.0	–	0.56	−1.00	0.56	–	−0.07	−0.04	–
	1.2	–	1.01	−1.00	0.69	–	−0.58	−0.12	–
	2.0	0.01	0.66	−1.00	0.74	–	−0.46	0.07	–
	10	1.26	1.19	−1.00	1.22	–	−0.14	−0.01	–
	50	3.13	2.10	−1.00	2.12	–	−0.11	0.01	–
He	1.0	–	0.13	−1.00	0.28	0.38	–	0.21	–
	1.2	–	0.03	−1.00	0.34	0.52	–	0.10	–
	2.0	–	0.23	−1.00	0.37	0.48	–	−0.07	–
	10	0.28	0.33	−1.00	0.60	0.32	–	0.01	0.01
	50	2.64	0.56	−1.00	1.06	0.34	–	−0.04	1.73
O	1.0	–	0.04	−1.00	0.21	0.25	−0.25	0.76	–
	1.2	–	–	−1.00	0.28	1.06	−0.91	0.57	–
	2.0	–	0.06	−1.00	0.29	1.20	−0.17	−0.38	–
	10	0.26	0.08	−1.00	0.48	0.78	−0.03	−0.06	0.01
	50	2.42	0.14	−1.00	0.83	0.63	0.30	−0.29	1.81

I, inertia; P, partial pressure; G; gravity; E, electric force; C_p, proton drag; C_α, helium drag; T, thermal force; R, rotational forces.
Terms smaller than 0.01 have been omitted.

mass proportional: in this case the pressure for all ions would have the same relative magnitude as for the protons and the velocity thus get much closer to U_p. Since ion temperatures equilibrate relatively fast, we expect nearly equal temperatures in the dense corona. We assume in our model calculations that the transition to $T \sim A$ occurs only at a relatively large solar distance. A transition distance of $\simeq 10\, R_\odot$ would have no appreciable effect on the charge state distributions. However, the velocities of the heavier ions would be significantly augmented due to (a) the increased pressure term (cf. Table IV), and (b) the momentum transfer from the waves that provide the heating.

The electric force, which goes as Z/A, contributes significantly to the acceleration of all ions, though less for the heavier, not fully charged ones. The proton drag is a dominant term in the acceleration of heavy ions, although in the region of highest He-enhancement it is nearly compensated by the helium drag. In the corona, the helium drag also contributes significantly to the retarding force on the protons. Thermal diffusion is strong for highly charged heavy ions in the low corona, but becomes unimportant beyond a few solar radii, mainly because of the strong velocity cut-off (cf. Equation (28)). Inertial and rotational forces are significant only at large distances. The acceleration term I is equal to the sum of all the other terms (apart from rounding errors) as it should be. The finding that the friction with α-particles can be significant both for protons and minor ions is again in agreement with the results and conclusions of Joselyn and Holzer (1978).

Finally we have investigated the possibility for isotope separation in the corona. We

cannot, of course, derive abundances in a steady state model, especially not in the minor ion approximation, as discussed by Borrini and Noci (1979). We can conclude, however, that differentiation of elements or isotopes may only occur if their dynamical behaviour differs significantly. Figure 10 shows the flow speeds for ^{3}He, ^{4}He, ^{20}Ne, and ^{22}Ne in the corona. There is in fact a considerable difference between the two helium isotopes, but almost none for neon. Thus isotope fractionation in the corona is likely to occur for helium, but not for any other pair of isotopes of significant abundance, since all other such pairs have a smaller relative mass difference than ^{20}Ne/^{22}Ne.

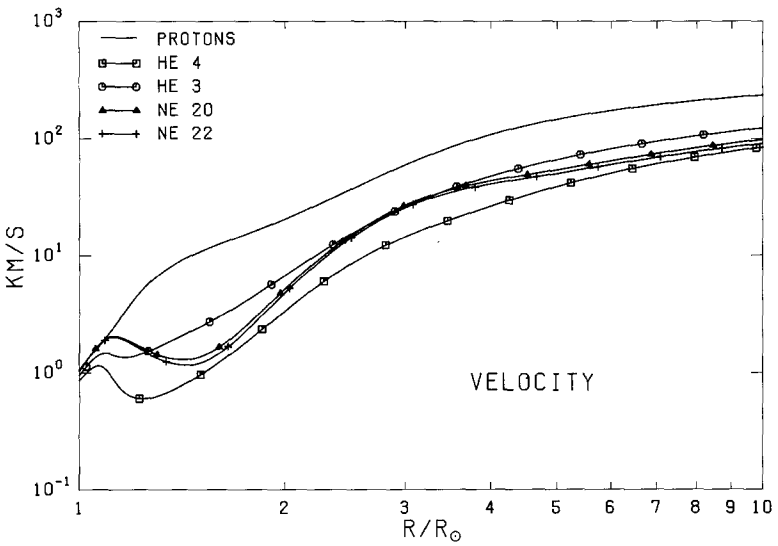

Fig. 10. Velocity solutions for isotopes of He and Ne in Model 4. There is a considerable difference in the dynamics of the He isotopes, but almost none for Ne.

9. Model 5: Wave-Driven High Speed Solar Wind

Munro and Jackson (1977) have presented a model for a coronal hole and derived velocity and temperature profiles from observed electron density (the procedure that we also have adopted in this work) assuming a thermally driven solar wind (no wave pressure). The most striking result was a very high temperature ($> 3 \times 10^6$ K) in the range 3–5 $R_\odot$.

A thermally driven model (Model 3) did not provide sufficient Coulomb drag for acceleration of heavy ions such as oxygen (Figure 5), and for models with higher speed (and thus higher temperature in the thermal case) the drag would be even lower (cf. Equation (40)). Also, we would encounter serious difficulties when trying to model two-fluid solutions, as they would imply a tremendous He-enhancement throughout the corona, as well as travel times for ^{4}He of the order of 100 days. Thus, unless ion temperatures were mass-proportional right from the coronal base, thermally driven

models tend to predict the absence of heavy ions from the high speed solar wind, which is contrary to observation. Furthermore, it is well documented by both *EUV* observations (cf. Huber *et al.*, 1974) and charge state measurements in the solar wind (Ipavich *et al.*, 1985) that coronal holes are colder than the surrounding corona. The explanation at hand is that high speed streams are not only thermally driven, but that wave pressure also contributes significantly to their acceleration. In fact Alfvén waves have been observed by Belcher and Davis (1971) to be particularly strong in high speed streams.

We have fitted a density profile to the polar coronal hole data of Allen (1973), which cover a larger radial range than the Munro and Jackson data, but agree well with them in the region of overlap. We have then multiplied these densities by two, to obtain a profile more appropriate to the somewhat denser equatorial coronal holes (cf. Saito *et al.*, 1977). The boundary value at 1 AU was taken to be $n_e = 4\ \mathrm{cm}^{-3}$. Due to the lack

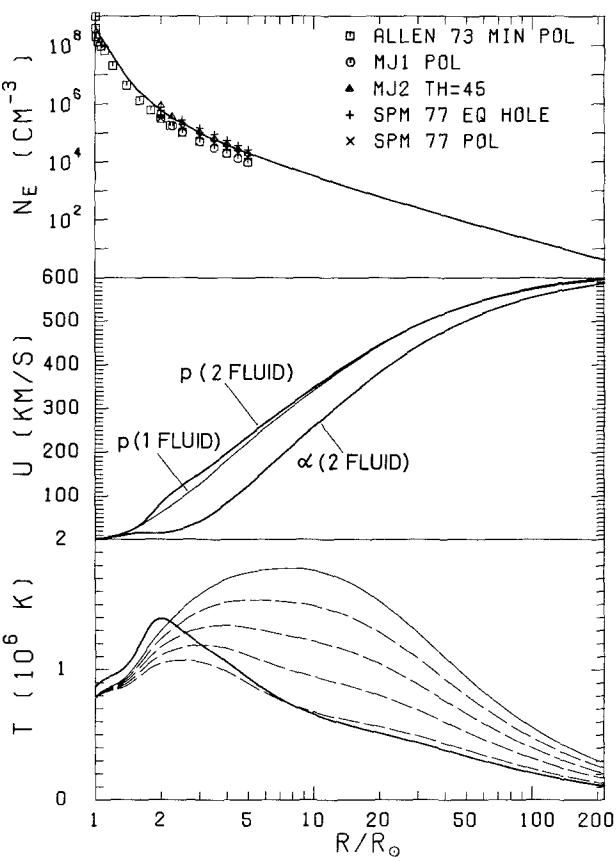

Fig. 11. The model for the wave-driven coronal hole (Model 5, solid thick line). Also shown is a corresponding, but thermally driven one-fluid model (thin line), and one-fluid models with incoming wave flux of 20% (uppermost dashed line), 40, 60, and 80% (lowest dashed line) of the proton kinetic energy at 1 AU. The electron density data are from Allen (1973) for the polar corona at solar minimum, the coronal hole of Munro and Jackson (1977) at the pole (MJ1) and at $\vartheta = 45°$ (MJ2), and from Saito *et al.* (1977) for an equatorial and a polar coronal hole (SPM).

of other data, we adopted the geometry of the polar coronal hole observed by Munro and Jackson (1977), with the parameters (rounded numbers)

$$f_m = 7.5, \qquad \sigma_1 = 0.5\,R_\odot, \qquad r_1 = 1.3\,R_\odot \tag{49}$$

(cf. Equation (2)). We chose a flow speed of 600 km s^{-1} at 1 AU as boundary condition, and $F_\alpha/F_p = 0.04$. The magnetic field was taken to be $B_0 = 7.5$ G at $R_\odot$, which gives the Alfvén critical radius at 11.3 $R_\odot$, consistent with the lower bound given by Marsch and Richter (1984). Only the proton density is taken into account in calculating the Alfvén speed (cf. Section 7.1). Taking into account helium as well would change the results somewhat quantitatively, not qualitatively, but greatly increase computational complexity.

The remaining free parameter is the wave energy flux entering the corona from below,

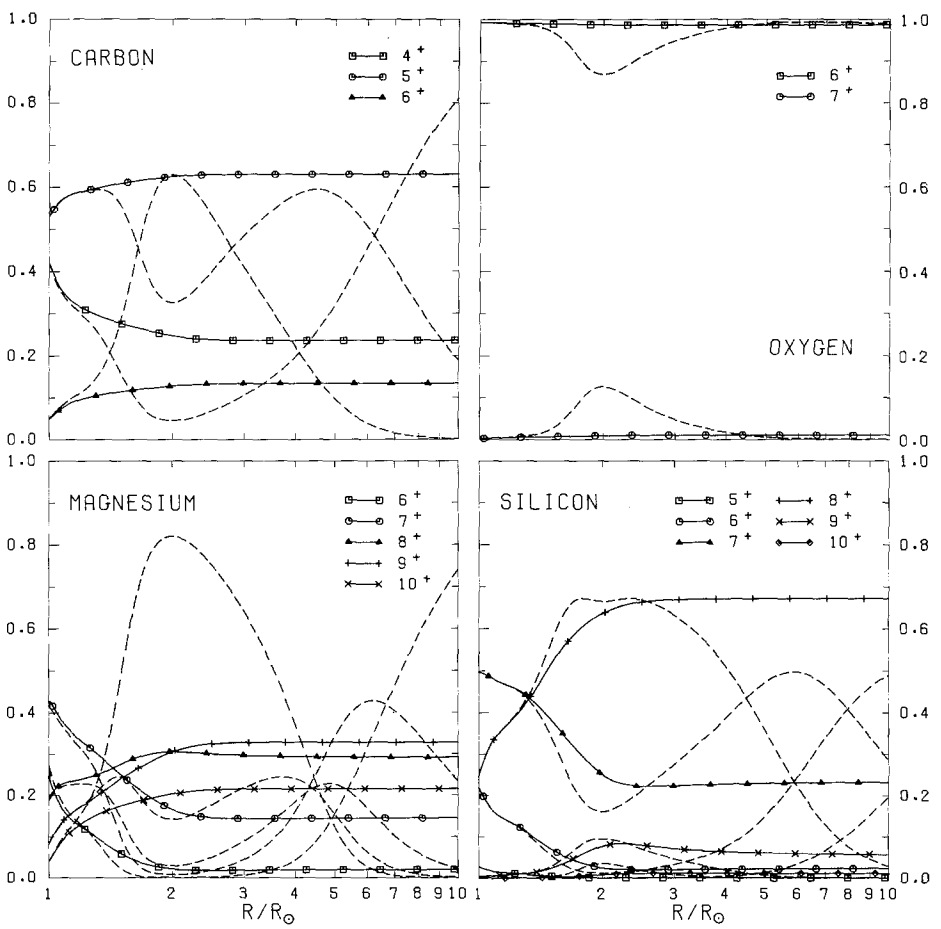

Fig. 12. Solutions for charge states of C, O, Mg, and Si in Model 5 (wave-driven coronal hole, two-fluid). Due to the low density, all ions depart from local equilibrium (dashed lines) at low solar altitude, and are essentially frozen-in below the temperature maximum.

which we took to be 1.78×10^5 erg cm^{-2} s^{-1}, corresponding to 80% of the proton kinetic energy flux at 1 AU. The result for the main gas of Model 5 are plotted in Figure 11. We get a relatively cool corona with $T_{max} = 1.39 \times 10^6$ K at 2.1 $R_\odot$. Also plotted are the profiles for a thermally driven one-fluid model (no waves) and one-fluid models with wave energy fluxes of 20, 40, 60, and 80% of the proton kinetic energy at 1 AU. The model without waves resembles the Munro and Jackson model, except that its speed and temperature are lower. Figure 11 shows how the increasing wave power decreases the temperatures that one obtains from a given n_e profile.

9.1. Minor ions in Model 5: charge states

Figure 12 shows charge state profiles for C, O, Mg, and Si in Model 5. It is seen that all charge states freeze-in before the plasma gets to the temperature maximum, because the density is low and the maximum is relatively far from the Sun.

The frozen-in charge states and the corresponding freezing-in temperatures are shown in Table V. Compared to Model 4 the distribution has shifted to lower charges. The freezing-in temperatures are low, though not much below the 1.4×10^6 K observed by Ipavich *et al.* (1986) for iron charge states in the high speed solar wind. The trend among freezing-in temperatures has reversed compared to Model 4: higher charge states now freeze-in at lower temperature (cf. the results for C and Mg in Table V), which is the signature of freezing-in on the rising part of the temperature profile.

TABLE V

Frozen-in charge states in the two-fluid Model 5 (wave-driven coronal hole model)

Ion	Relative abundance	Freezing-in temperature (10^6 K)	Ion	Relative abundance	Freezing-in temperature (10^6 K)
C^{4+}	0.24	1.09	Mg^{6+}	0.02	1.24
C^{5+}	0.63	0.97	Mg^{7+}	0.15	1.20
C^{6+}	0.13		Mg^{8+}	0.29	1.03
N^{5+}	0.84	0.99	Mg^{9+}	0.33	0.91
N^{6+}	0.16		Mg^{10+}	0.22	
O^{6+}	0.99		Si^{6+}	0.02	1.26
Ne^{7+}	0.03	1.17	Si^{7+}	0.23	1.27
Ne^{8+}	0.97		Si^{8+}	0.67	1.23
			Si^{9+}	0.06	1.24
			Si^{10+}	0.01	

Cf. comments to Table III.

However, these results for charge states are somewhat questionable, since two of our assumptions become critical in the low density of a coronal hole, i.e., the assumptions of Maxwellian electron distribution (ionization rates) and the assumption of equal velocity of charge states. Some of the freezing-in temperatures might easily be modified, and probably shifted to higher values, if tails in the electron velocity distribution or

differential velocities between charge states played an important role (Owocki, 1982; Owocki and Scudder, 1983; Owocki *et al.*, 1983).

9.2. Minor ions in model 5: velocities

The velocities of the major and some minor ions (C, O, Mg, Si) are plotted in Figure 13. Beyond several $R_\odot$, all minor ion velocities converge towards the helium velocity, which in turn almost reaches U_p at large distances. Still, He and minor ions cannot be accelerated to $u > U_p$ by nonresonant waves alone (McKenzie *et al.*, 1979), and a resonant interaction has to be invoked to give $u > U_p$.

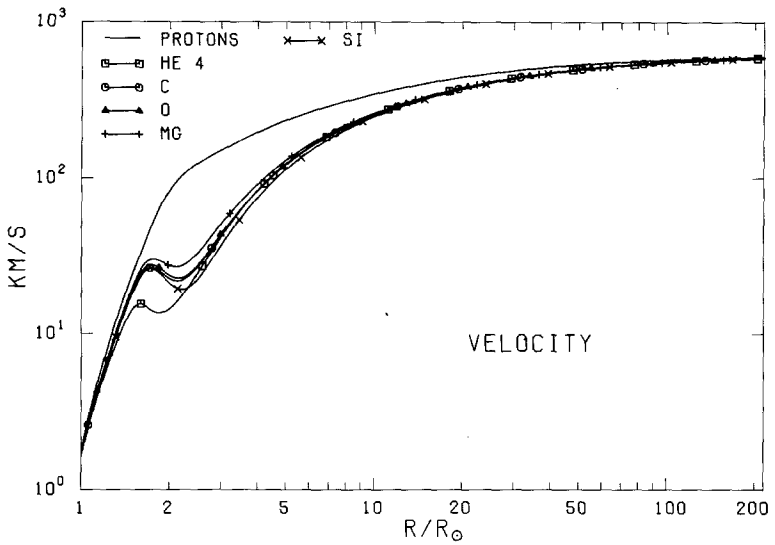

Fig. 13. Solutions for the velocities of H, He, C, O, Mg, and Si in Model 5 (wave-driven coronal hole, two-fluid).

Although parameters characterizing the waves have been chosen so as to maximize wave acceleration even at small heliocentric distances (large wave energy flux and low Alfvén critical point), all heavy ions are still markedly slower than protons in the radial range 1.5–5 $R_\odot$, since the wave force is ineffective for $U \ll V_A$. Unless a resonant wave force operates so near to the Sun, we expect that local densities of ions heavier than protons are enhanced in this part of the corona.

The influence of waves on minor ions is twofold: besides the direct acceleration, waves also give lower temperatures compared to a purely thermal model. Only at low temperatures are Coulomb collisions strong enough to accelerate the heavy ions through the first few $R_\odot$ after which waves can further accelerate them.

Table VI lists the relative strength of the individual terms in the momentum equations of H, He, and O in Model 5. As in Model 4, pressure and electric field become less important with increasing mass. Since the density is lower and the coronal He-enhancement less pronounced, both proton and helium drag are less effective than in Model 4.

TABLE VI

Relative importance of terms in the momentum equation of H, He, and O in Model 5, normalized to gravity

Element	$r/R_\odot$	I	P	G	E	C_p	C_α	T	R	W
H	1.0	–	0.55	−1.00	0.55	–	−0.09	−0.01	–	0.01
	2.0	0.20	0.71	−1.00	0.66	–	−0.34	–	–	0.16
	5.0	1.06	0.67	−1.00	0.69	–	−0.06	–	–	0.76
	10	2.80	0.81	−1.00	0.82	–	−0.04	–	–	2.21
	50	10.1	1.99	−1.00	1.99	–	−0.03	–	–	7.18
He	1.0	–	0.13	−1.00	0.27	0.52	–	0.06	–	0.01
	2.0	–	0.14	−1.00	0.33	0.37	–	–	–	0.16
	5.0	0.61	0.21	−1.00	0.34	0.21	–	−0.01	–	0.86
	10	2.61	0.22	−1.00	0.41	0.20	–	−0.01	–	2.78
	50	12.9	0.51	−1.00	0.99	0.18	–	−0.01	0.19	12.0
O	1.0	–	0.03	−1.00	0.20	0.72	−0.18	0.22	–	0.01
	2.0	−0.01	0.01	−1.00	0.25	0.79	−0.22	–	–	0.16
	5.0	0.60	0.05	−1.00	0.26	0.49	–	−0.07	–	0.86
	10	2.58	0.06	−1.00	0.31	0.47	–	−0.06	–	2.79
	50	13.0	0.13	−1.00	0.75	0.46	0.01	−0.03	0.20	12.4

I, inertia; P, partial pressure; G, gravity; E, electric force; C_p, proton drag; C_α, helium drag, T, thermal force; R, rotational forces; W, wave forces.
Terms smaller than 0.01 have been omitted.

Thermal diffusion is unimportant except at the lower boundary, while wave forces are by far dominant beyond the first few solar radii.

10. Conclusions

The conclusions of the work presented can be summarized as follows:

– One-fluid models do not give high coronal temperatures, and as a consequence they do not reproduce the charge state distributions observed in the solar wind at 1 AU.

– The reason for this failure of the one-fluid model is not the particular approach chosen here, but the fact that a consistent simultaneous modelling of major and minor ions taking into account measured density profiles in the corona and solar wind data at 1 AU imposes more constraints on solar wind models.

– These constraints would be further tightened if additional observations were available, e.g., data on densities and speeds of the coronal plasma, magnetic field configurations in the source region of the solar wind, and more comprehensive data on abundances and charge states in the solar wind.

– The two-fluid model for the low speed solar wind reproduces the observed charge state distributions, especially the ratio O^{6+}/O^{7+}, for which a freezing-in temperature $\simeq 1.6 \times 10^6$ K is obtained. Freezing-in temperatures for most other ion pairs are usually somewhat lower, consistent with the scarce observations available so far.

TABLE VII

Summary of model parameters and results

Model	n_e profile	F_α/F_p	1 AU			Geometry	T_{max} (10^6 K)	$r(T_{max})$ ($R_\odot$)	B_0 (gauss)	r_A[d] ($R_\odot$)
			n_e (cm^{-3})	U_p (km s^{-1})	n_pU_p (10^8 cm^{-2} s^{-1})					
1	Minimum corona[a]	0	10	360	3.60	radial	1.23	1.25	3.0	29.4
1A	Minimum corona	0	8	360	2.88	radial	1.23	1.25	3.0	33.5
1B	Minimum corona	0	12	360	4.32	radial	1.23	1.25	3.0	26.5
1C	Minimum corona	0	10	330	3.30	radial	1.23	1.25	3.0	31.9
1D	Minimum corona	0	10	390	3.90	radial	1.23	1.25	3.0	27.4
2	Streamer B_2[b]	0	10	300	4.50	radial	1.57	1.28	3.0	30.8
3	Coronal hole[c]	0	15	400	2.40	radial	1.53	3.23	2.0	22.2
4	Minimum corona	4%	6	363	3.31	Equation (48)	2.00	1.30	10	32.5
4A	Minimum corona	2%	10	362	2.76	Equation (48)	2.31	1.25	10	36.9
4B	Minimum corona	4%	8	364	3.98	Equation (48)	1.62	1.32	10	29.3
4C	Minimum corona	4%	12	332	3.04	Equation (48)	2.22	1.28	10	35.3
4D	Minimum corona	4%	10	395	3.59	Equation (48)	1.80	1.32	10	30.2
5	Coronal hole[c], wave driven	4%	10 4	597	2.21	Equation (49)	1.39	2.00	7.5	11.3

[a] Saito, 1970: minimum corona, equator.
[b] Saito, 1972.
[c] Allen, 1973; minimum corona, pole, n_e doubled.
[d] Alfvén point.

– In a thermally driven coronal hole model the Coulomb drag seems to be insufficient to accelerate heavy ions into the solar wind. If non-resonant momentum transfer of waves is included, acceleration of heavier ions occurs and freezing-in temperatures lower than those in the slow solar wind are obtained in general agreement with observation. However, the freezing-in results depend critically on the validity of our assumptions.

– The models give $u \leqq U_p$ for all heavy ions. We propose that this is a real effect in the corona, and that the local density of heavy ions is enhanced there, up to the degree predicted by the steady state model. Near the temperature maximum helium will be particularly enhanced, there the models give He/H in the range 0.2–0.7. However, the larger values may not actually occur.

– In the wave-driven coronal hole model, the speeds of heavy ions converge towards the proton speed for large distances, whereas the models for the low speed solar wind give $u < U_p$. We agree with other authors that $u > U_p$ as is observed results from resonant wave particle interactions in outer corona and/or interplanetary space. This question is not addressed in the present paper.

– Isotope separation in the corona is possible for helium isotopes, but ought to be ineffective for neon and most other elements.

– Finally, we emphasize that the influence of parameters or boundary conditions in our model does not reflect physical causality. Many of our parameter studies were performed with a fixed electron density, whereas a change in the dynamics or energetics of the solar wind source would certainly affect these profiles as well. Thus, we do not mean to imply that a helium enhancement actually heats the corona (Section 7.5), or that waves cool the solar wind (discussion of Figure 11).

The most serious limitations of our models, which could be improved upon in future work, seem to us:

– The assumption of equal temperatures, especially $T_p = T_e$. This assumption in fact becomes critical very low in the corona, i.e., in the freezing-in region of the charge states. With $T_e \neq T_p$ the electron temperature profile would tend to be flatter than what we infer, due to the high thermal conductivity of electrons. Relaxing this assumption would require a correct treatment of the energy equations, however, with all the complexities and uncertainties of heat fluxes and energy sources.

– Allowing for differential speeds between charge states might in certain cases significantly modify the calculated charge state distributions. However, this would require the solution of a coupled system of very nonlinear differential equations, and thus an elaborate treatment of a multitude of interdependent critical points.

Acknowledgements

The authors wish to thank Drs P. Bochsler and G. Beutler for helpful discussions. This work was supported by the Swiss National Science Foundation.

References

Alazraki, G. and Couturier, P.: 1971, *Astron. Astrophys.* **13**, 380.

Allen, C. W.: 1973, *Astrophysical Quantities*, 3rd ed., Athlone Press, London.

Bame, S. J., Asbridge, J. R., Feldman, W. C., and Kearney, P. D.: 1974, *Solar Phys.* **35**, 137.

Bame, S. J., Asbridge, J. R., Feldman, W. C., and Gosling, J. T.: 1977, *J. Geophys. Res.* **82**, 1487.

Belcher, J. W.: 1971, *Astrophys. J.* **168**, 509.

Belcher, J. W. and Davis, L.: 1971, *J. Geophys. Res.* **76**, 3534.

Beutler, G.: 1979, *Mitteilung der Satelliten-Beobachtungsstation Zimmerwald*, No. 4, Bern.

Bochsler, P.: 1983, in M. Neugebauer (ed.), *Solar Wind Five, NASA Conf. Publ.*, No. 2280, 613.

Bochsler, P.: 1984, 'Helium and Oxygen in the Solar Wind: Dynamic Properties and Abundances of Elements and Helium Isotopes as Observed with the ISEE-3 Plasma Composition Experiment', Habilitation Thesis, University of Bern.

Bochsler, P., Geiss, J., and Joos, R.: 1985, *J. Geophys. Res.* **90**, 10779.

Borrini, G. and Noci, G.: 1979, *Solar Phys.* **64**, 367.

Borrini, G., Gosling, J. T., Bame, S. J., Feldman, W. C., and Wilcox, J. M.: 1981, *J. Geophys. Res.* **86**, 4565.

Borrini, G., Gosling, J. T., Bame, S. J., Feldman, W. C.: 1982, *J. Geophys. Res.* **87**, 7370.

Burgers, J. M.: 1969, *Flow Equations for Composite Gases*, Academic Press, New York.

Bürgi, A.: 1984, Ionisation and Beschleunigung von seltenen Elementen in Korona und Sonnenwind, Ph.D. Thesis, University of Bern.

Couturier, P.: 1977, *Astron. Astrophys.* **59**, 239.

Cuperman, S. and Metzler, N.: 1975, *Astrophys. J.* **196**, 205.

Cuperman, S., Harten, A., and Dryer, M.: 1972, *Astrophys. J.* **177**, 555.

Cuperman, S., Weiss, I., and Dryer, M.: 1980, *Astrophys. J.* **239**, 345.

Cuperman, S., Metzler, N., and Dryer, M.: 1981a, *Astrophys. Space Sci.* **79**, 67.

Cuperman, S., Weiss, I., and Dryer, M.: 1981b, *Astrophys. J.* **251**, 297.

Dewar, R. L.: 1970, *Phys. Fluids* **13**, 2710.

Feldman, W. C., Asbridge, J. R., Bame, S. J., Gosling, J. T., and Lemons, D. S.: 1979, *J. Geophys. Res.* **84**, 6621.

Fort, B., Picat, J. P., Combes, M., and Felebok, P.: 1972, *Astron. Astrophys.* **17**, 55.

Geiss, J., Hirt, P., and Leutwyler, H.: 1970, *Solar Phys.* **12**, 458.

Gosling, J. T., Borrini, G., Asbridge, J. R., Bame, S. J., Feldman, W. C., and Hansen, R. T.: 1981, *J. Geophys. Res.* **86**, 5438.

Hirshberg, J., Asbridge, J. R., and Robbins, D. E.: 1972, *J. Geophys. Res.* **77**, 3583.

Hollweg, J. V.: 1974, *J. Geophys. Res.* **79**, 1539.

Hollweg, J. V.: 1976, *J. Geophys. Res.* **81**, 1649.

Huber, M. C. E., Foukal, P. V., Noyes, R. W., Reeves, E. M., Schmahl, E. J., Timothy, J. G., Vernazza, J. E., and Withbroe, G. L.: 1974, *Astrophys. J.* **194**, L115.

Hundhausen, A. J.: 1972, *Coronal Expansion and Solar Wind*, Springer, Berlin.

Hundhausen, A. J., Gilbert, H. E., and Bame, S. J.: 1968, *Astrophys. J.* **152**, L3.

Ipavich, F. M., Galvin, A. B., Gloeckler, G., Hovestadt, D., Bame, S. J., Klecker, B., Scholer, M., Fisk, L. A., and Fan, C. Y.: 1986, *J. Geophys. Res.* (in press).

Isenberg, P. A. and Hollweg, J. V.: 1983, *J. Geophys. Res.* **88**, 3923.

Jacques, S. A.: 1977, *Astrophys. J.* **215**, 942.

Joselyn, J. and Holzer, T. E.: 1978, *J. Geophys. Res.* **83**, 1019.

Kopp, R. A. and Holzer, T. E.: 1976, *Solar Phys.* **49**, 43.

Koutchmy, S.: 1972, *Solar Phys.* **24**, 373.

Koutchmy, S.: 1977, *Solar Phys.* **51**, 399.

Krieger, A. S., Timothy, A. F., and Roelof, E. C.: 1973, *Solar Phys.* **29**, 505.

Kunz, S., Bochsler, P., Geiss, J., Ogilvie, K. W., and Coplan, M. A.: 1983, *Solar Phys.* **88**, 359.

Marsch, E. and Richter, A. K.: 1984, *J. Geophys. Res.* **89**, 5386.

Marsch, E., Mühlhäuser, K. H., Rosenbauer, H., Schwenn, R., and Neubauer, F. M.: 1982a, *J. Geophys. Res.* **87**, 35.

Marsch, E., Goertz, C. K., and Richter, K.: 1982b, *J. Geophys. Res.* **87**, 5030.

McKenzie, J. F., Ip, W.-H., and Axford, W. I.: 1979, *Astrophys. Space Sci.* **64**, 183.

Metzler, N. and Dryer, M.: 1978, *Astrophys. J.* **222**, 689.
Muhleman, D. O., Esposito, P. B., and Anderson, J. D.: 1977, *Astrophys J.* **211**, 943.
Munro, R. H. and Jackson, B. V.: 1977, *Astrophys. J.* **213**, 874.
Nakada, M. P.: 1970, *Solar Phys.* **14**, 475.
Neugebauer, M.: 1981, in H. Rosenbauer (ed.), *Solar Wind Four*, MPAE–W–100–81–31, p. 425
Noci, G. and Porri, A.: 1983, 'Models of the Solar Wind Acceleration Region', paper 4L.04 presented at the 18th General Assembly Meeting, IAGA, Hamburg, 1983.
Nolte, J. T., Krieger, A. S., Timothy, A. F., Gold, R. E., Roelof, E. C., Vaiana, G., Lazarus, A. J., Sullivan, J. D., and McIntosh, P. S.: 1975, *Solar Phys.* **46**, 303.
Ogilvie, K. W. and Scudder, J. D.: 1978, *J. Geophys. Res.* **83**, 3776.
Ogilvie, K. W. and Vogt, C.: 1980, *Geophys. Res. Letters* **7**, 577.
Ogilvie, K. W., Coplan, M. A., and Zwickl, R. D.: 1982, *J. Geophys. Res.* **87**, 7363.
Owocki, S. P.: 1982, *The Ionization State of the Solar Wind*, Nat. Center Atm. Res. CT-66.
Owocki, S. P. and Scudder, J. D.: 1983, *Astrophys. J.* **270**, 758.
Owocki, S. P., Holzer, T. E., and Hundhausen, A. J.: 1983, *Astrophys. J.* **275**, 354.
Patchett, B. E., Norman, K., Gabriel, A. H., and Culhane, J. L.: 1981, *Space Sci. Rev.* **29**, 431.
Saito, K.: 1970, *Ann. Tokyo Astron. Obs., Ser. 2*, **12**, 53.
Saito, K.: 1972, *Ann. Tokyo Astron. Obs., Ser. 2*, **13**, 93.
Saito, K., Poland, A. I., and Munro, R. H.: 1977, *Solar Phys.* **55**, 121.
Salat, A.: 1975, *Plasma Phys.* **17**, 589.
Schmidt, W. K. H., Rosenbauer, H., Shelley, E. G., and Geiss, J.: 1980, *Geophys. Res. Letters* **7**, 697.
Schunk, R. W.: 1975, *Planetary Space Sci.* **23**, 437.
Schunk, R. W. and Walker, J. C. G.: 1969, *Planetary Space Sci.* **17**, 853.
Scudder, J. D. and Olbert, St.: 1979a, *J. Geophys. Res.* **84**, 2755.
Scudder, J. D. and Olbert, St.: 1979b, *J. Geophys. Res.* **84**, 6603.
Sheeley, N. R. Jr., Harvey, J. W., and Feldman, W. C.: 1976, *Solar Phys.* **49**, 271.
Shull, J. M. and Van Steenberg, M.: 1982, *Astrophys. J. Suppl.* **48**, 95, and **49**, 351 (with erratum).
Sittler, E. C.: 1978, 'Study of the Electron Component of the Solar Wind and Magnetospheric Plasma', Ph.D. Thesis, M.I.T., Cambridge.
Spitzer, L.: 1956, *Physics of Fully Ionized Gases*, Interscience Publishers, New York.
St. Maurice, J.-P. and Schunk, R. W.: 1977, *Planetary Space Sci.* **25**, 907.
Steinolfson, R. S. and Tandberg-Hansen, E.: 1977, *Solar Phys.* **55**, 99.
Weber, E. J. and Davis, L.: 1967, *Astrophys. J.* **148**, 217.
Withbroe, G. L., Kohl, J. L., Weiser, H., Noci, G., and Munro, R. H.: 1982, *Astrophys. J.* **254**, 361.
Zastenker, G. N. and Yermolaev, Yu. I.: 1981, *Planetary Space Sci.* **29**, 1235.